JGR Solid Earth

RESEARCH ARTICLE
10.1029/2025JB032659

Reconstructing Late Pleistocene to Prehistorical Holocene Geomagnetic Field Variations From La Palma Lava Flows (Canary Islands, Spain): Unraveling Viscous Components

Eva Vernet[1], Manuel Calvo-Rathert[1], Ángel Carrancho[2], Yuhji Yamamoto[3], Lidia Rodríguez-Méndez[4], Josep M. Parés[5], and Vicente Soler[6]

[1]Departamento de Física, EPS, Universidad de Burgos, Burgos, Spain, [2]Área de Prehistoria, Departamento de Historia, Geografía y Comunicación, Universidad de Burgos, Burgos, Spain, [3]Marine Core Research Institute, Kochi University, Kochi, Japan, [4]Departamento de Geología, Facultad de Ciencia y Tecnología, Universidad del País Vasco/Euskal Herriko Univertsitatea UPV/EHU, Leioa, Spain, [5]Geochronology & Geology, CENIEH, Burgos, Spain, [6]Instituto de Productos Naturales y Agrobiología (IPNA), La Laguna, Spain

Abstract We present new vector paleomagnetic data from 13 radiometrically dated lava-flows in southern La Palma (Canary Islands) spanning from 1 to 56 ka, which covers most of the Late Pleistocene to prehistoric Holocene volcanic record in the island. Using a paleointensity multimethod approach including Thellier-type and Shaw-type techniques, and combining detailed rock magnetic and mineralogical analyses, we assess the reliability and possible biases in paleointensity estimations in volcanic rocks affected by low-temperature oxidation and coarse ferromagnetic grains. Results indicate a strong viscous component linked to maghemitization, which compromises paleointensity reliability and accuracy. Low temperature demagnetization pretreatments significantly mitigated the viscosity contribution, improving success rates by highlighting the original thermoremanent magnetization (TRM) and revealing possible overestimations in standard Thellier-type treated samples affected by maghemitization. The full vector results, compared with several paleosecular variation curves, exhibited both low and high field intensity periods, including a relative paleointensity minimum at ~27 ka (VADM ~26 ZAm^2) and the record of the Levant intensity high (VADM ~108 ZAm^2). This study contributes with valuable constraints for improving geomagnetic models, especially for low-latitude regions, and underscores the importance of integrating magnetic mineralogy with paleointensity protocols to mitigate bias in geomagnetic reconstructions.

Plain Language Summary We studied lava flows from southern La Palma, in the Canary Islands, that erupted between 1,000 and 56,000 years ago. These rocks recorded information about the Earth's magnetic field at the time they formed. We used several laboratory methods to estimate the direction (paleomagnetic directions) and strength of the ancient magnetic field (paleointensity), including techniques that can detect and correct problems caused by chemical changes in the rocks over time. One common issue we found was a magnetic effect caused by the oxidation of minerals, which can lead to inaccurate results. However, we were able to improve the accuracy of our data by applying a low-temperature pretreatment step with liquid nitrogen before measuring. Our results revealed evidence of a relative minimum in Earth's magnetic field intensity 27,000 years ago, as well as an unusually high-intensity event documented in Europe 3,000 years ago. This research adds important data from a low latitude region, which helps build more accurate models of Earth's magnetic field changes through time.

Key Points:

- New paleomagnetic data from La Palma lava flows (1–56) ka with paleointensity multimethod approach: Thellier-type and Shaw-type
- Rock magnetism links maghemitization as main cause of viscous remanences, reduced through LTD pretreatment applied to Thellier-Coe
- Paleointensity results reveal distinct geomagnetic features: the Levantine high (3 ka) and a relative paleointensity minimum (~27 ka)

Supporting Information:

Supporting Information may be found in the online version of this article.

Correspondence to:

E. Vernet,
evernet@ubu.es

Citation:

Vernet, E., Calvo-Rathert, M., Carrancho, Á., Yamamoto, Y., Rodríguez-Méndez, L., Parés, J. M., & Soler, V. (2026). Reconstructing Late Pleistocene to prehistorical Holocene geomagnetic field variations from La Palma lava flows (Canary Islands, Spain): Unraveling viscous components. *Journal of Geophysical Research: Solid Earth*, *131*, e2025JB032659. https://doi.org/10.1029/2025JB032659

Received 4 AUG 2025
Accepted 8 JAN 2026

Author Contributions:

Conceptualization: Eva Vernet, Manuel Calvo-Rathert, Ángel Carrancho
Data curation: Eva Vernet, Manuel Calvo-Rathert, Ángel Carrancho, Yuhji Yamamoto, Lidia Rodríguez-Méndez
Formal analysis: Eva Vernet, Yuhji Yamamoto
Funding acquisition: Manuel Calvo-Rathert, Ángel Carrancho,

1. Introduction

Paleomagnetic data are essential for understanding past variations of the Earth's magnetic field, providing valuable insights into the dynamics of the geodynamo operating within the Earth's outer core. Full vector paleomagnetic records from well-dated samples offer critical information about paleosecular variation (PSV), particularly in regions and time periods where data remain scarce. Despite efforts to build global paleomagnetic databases, low-latitude regions like Africa remain poorly documented (Di Chiara, 2019; Nilsson et al., 2014). Previous investigations have highlighted the contribution of the Canary Islands, located at latitudes 27°–29°N, to capture potential non-dipolar field contributions (e.g., Kissel, Laj, et al., 2015; Kissel, Rodriguez-Gonzalez, et al., 2015; Monster et al., 2018) and better constrain the timing and geographic extent of geomagnetic instabilities and anomalies (Singer, 2014).

Yuhji Yamamoto, Lidia Rodríguez-Méndez
Investigation: Eva Vernet
Methodology: Eva Vernet, Yuhji Yamamoto
Resources: Eva Vernet, Manuel Calvo-Rathert, Ángel Carrancho, Yuhji Yamamoto, Lidia Rodríguez-Méndez, Josep M. Parés, Vicente Soler
Software: Yuhji Yamamoto
Supervision: Manuel Calvo-Rathert, Ángel Carrancho, Yuhji Yamamoto
Validation: Eva Vernet, Manuel Calvo-Rathert, Ángel Carrancho, Yuhji Yamamoto
Visualization: Eva Vernet, Lidia Rodríguez-Méndez
Writing – original draft: Eva Vernet
Writing – review & editing: Eva Vernet, Manuel Calvo-Rathert, Ángel Carrancho, Yuhji Yamamoto, Lidia Rodríguez-Méndez

Precisely dated volcanic rocks are the only materials that enable the determination of absolute paleointensity over geological timescales. Therefore, La Palma lava-flows provide an ideal setting for addressing gaps in both paleomagnetic and paleointensity records for the last millennia, due to the availability of isotopically dated lava flows and a well-preserved volcanic record. However, the reliability of such geomagnetic features depends heavily on the magnetic mineralogy and stability of the recorded thermomagnetic remanence. The complexity in obtaining consistent paleointensity results can be of particular importance in volcanic samples affected by low-temperature oxidation or coarse magnetic grains (e.g., Monster et al., 2015). Detailed rock magnetic analyses combined with a multimethod paleointensity approach, based on different principles, considerably improve paleointensity reliability and reveal potential biases (e.g., Calvo-Rathert et al., 2024).

This study presents new paleomagnetic directions and absolute paleointensity estimations from 13 isotopically dated lava flows in southern La Palma, spanning from 1 to 56 ka, covering most of the Late Pleistocene to prehistoric Holocene volcanic record in the island. Furthermore, by integrating rock magnetic analyses with a multimethod paleointensity approach, we unravel the contribution of the viscous components' on paleointensity determinations and identify possible biases on paleointensity estimations. With this study, we aim to contribute to the understanding of the regional geomagnetic field behavior in the past millennia, as well as to discuss the reliability of the paleointensity method used in volcanic rocks affected by oxidation and coarse magnetic grains.

2. Geological Setting and Sampling

The Canary Islands archipelago is part of the over 100 seamounts forming the Canary Islands Seamounts Province (CISP), which extends along the NW African continent (Figure 1a). The CISP is related to an intraplate hotspot system, although its origin remains debated (e.g., Anguita et al., 2025; Courtillot et al., 2003). Van den Boogard (2013) proposed that a shallow mantle upwelling beneath the Atlantic Ocean basin of the NW African continental lithosphere flanks produced recurrent melting anomalies. This resulted in the formation of the CISP, which shows evidence of volcanism from the Late Jurassic to present, therefore, being the oldest hotspot track in the Atlantic Ocean, and the most long-lived preserved on Earth. Although records of Quaternary subaerial volcanism exist in all the Canary Islands except La Gomera, the largest volume of recently ejected material is found in La Palma and El Hierro (Ancochea et al., 2004), the westernmost islands of the archipelago (Figure 1b). These two islands remain in the juvenile shield stage, while the rest are already in post-erosional stages (Carracedo et al., 2001).

La Palma's geological history, extensively described by Carracedo et al. (2001), began in the Pliocene with the formation of a submarine complex of seamounts and associated plutonism, which, uplifted and tilted, conforms nowadays the basal complex (3–4 Ma; unit 1, Figure 1c). This was followed by the old volcanic series (1.7–0.41 Ma), which shaped the northern volcanic shield of the island (unit 2, Figure 1c), comprising the *Garafía*, *Taburiente* and *Bejenado* volcanoes. The *Taburiente* shield volcano emerged after the collapse of the *Garafía* complex and comprises the *Cumbre Nueva* rift zone. The volcanic activity after the gravitational landslide of the western flank of *Cumbre Nueva* that generated the *Caldera de Taburiente* (*ca.* 0.6 Ma), built the *Bejenado* stratovolcano. Subsequently, the volcanic activity was propagated toward the south at *ca*. 125 ka, generating the N-S trending ridge of *Cumbre Vieja* rift zone that remains active (unit 3, Figure 1c). This unit has been the most active volcano of the Canary Islands in historic times (Klügel et al., 2005), including the very recent *Tajogaite* eruption in 2021.

Improved radiometric dating of its volcanic rocks has clarified La Palma's recent volcanic history. The lava flows studied in this work comprise a very consistent record from 56 to *ca.* 1 ka. Lava flow ages and dating methods, obtained from Carracedo et al. (2001) and Guillou et al. (1998, 2001), are detailed in Table S1 of Supporting Information S1, and their distribution is shown in Figure 1c. Oriented samples were collected using a gasoline-powered drill, obtaining 6–12 cores per site, broadly distributed along the outcrops to minimize local magnetic anomalies (Valet & Soler, 1999). Cores were oriented using magnetic and sun compasses, and solar declination corrections (ranging from −17.4° to 0°) were calculated for each specimen when possible. In some cases, a mean declination correction per site was calculated and applied. Declination corrections were calculated using PMagTools. At protected site LPS12 Roque Teneguía, the sampling was performed by extracting three oriented blocks, obtaining their magnetic orientation in situ. In site LPS13 La Fajana only unoriented blocks were taken, as the paleomagnetic directions of this lava-flow have been previously studied by Monster et al. (2015). All samples

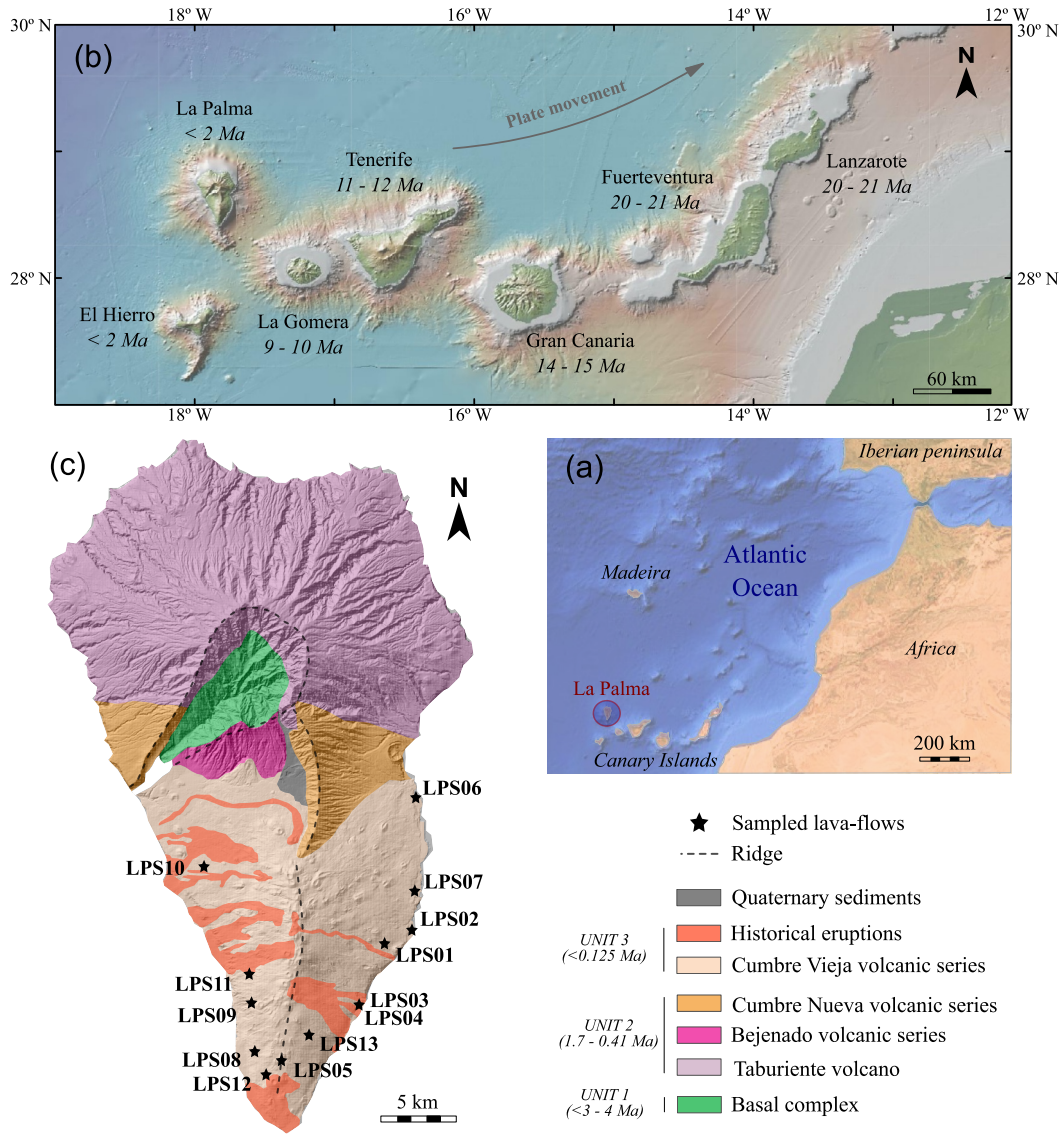

Figure 1. (a) Location of La Palma in the Canarian archipelago. (b) Oldest ages for the emerged volcanism of the Canarian archipelago and direction of the evolution of the hotspot (modified after Carracedo et al., 2001). (c) Location of the sampled lava-flows on La Palma simplified geological map (modified after Carracedo et al., 2001, Ancochea et al., 2004; Barker et al., 2015), where the units are: (1); the basal complex, (2); the northern shield, and (3); the southern ridge.

were cut into standard size specimens (10 cm^3) at the University of Burgos (UBU, Spain), preserving their magnetic orientation.

3. Laboratory Experiments

3.1. Magnetic Mineralogy

Several rock magnetic experiments were conducted to assess the suitability for paleomagnetic and paleointensity analyses, as well as to test the validity of the obtained results.

Coercivity and thermal analyses were conducted using a Variable Field Translation Balance (VFTB) at the UBU on 2–3 powdered specimens (~0.350 g) per lava-flow (29 in total). These experiments, carried out in air, included progressive isothermal remanent magnetization (IRM) acquisition and backfield curves, hysteresis loops (±1T)

and magnetization versus temperature curves up to 700°C under a 38 mT induced field. Data were processed with the RockMag Analyzer 1.1 software (Leonhardt, 2006).

Susceptibility *vs*. temperature curves (k-T) were conducted on one specimen per site (13 in total) after being powdered (∼0.350 g), with a Kappabridge KLY-4 (AGICO) connected to a CS3 furnace for high-temperature (40°C to 700°C) measurements, performed with Argon, and a CSL cryostat for low-temperature measurements (−195°C to 0°C) at the UBU. Results were analyzed with the Cureval8 software (Chadima & Hrouda, 2009).

First-Order Reversal Curves (FORCs; Pike et al., 1999) were measured on nine specimens, each from a different lava-flow, using a MicroMag 3,900 VSM at the Marine Core Research Institute (MaCRI, Japan). Measurements consisted of 200 acquired FORCs, with a saturating field of +1 T and a field increment of ∼1.5 mT, with a smoothing factor of 5 during the analyses. The data were processed with the FORCinel software (Harrison & Feinberg, 2008) using the simple smoothing option with a smoothing factor of 5 and an output grid spacing of 1.

To relate main mineralogical grain features to their magnetic behavior, eight representative samples of a range of magnetic behaviors observed were examined using a petrographic microscope under transmitted and reflected light. Polished thin sections were carbon-coated and analyzed using a JEOL JSM 7000F field-emission scanning electron microscope (FE-SEM). Energy-dispersive X-ray spectroscopy (EDX) was performed with an AZTEC Ultima Max 65 detector using a BSE signal at 20 kV, 1–3 nA, and a 10 mm working distance. Electron-backscatter diffraction (EBSD) was carried out using an AZTEC Symmetry S3 detector, at 3 nA with a variable working distance. These experiments were conducted at the University of the Basque Country, Spain.

Finally, thermal stability analyses were carried out to measure potential thermal alteration along the different heating steps applied during paleointensity experiments. One specimen per site was heated progressively under Argon in 19 different steps from room temperature up to 610°C, according to those performed for paleointensity experiments. Hysteresis and backfield curves were measured at room temperature after each temperature step. All measurements were conducted with a VFTB at the UBU. M_{rs}/M_s (saturation remanent magnetization vs. saturation magnetization) and B_{cr}/B_c (coercivity of remanence vs. coercivity) ratios were calculated for each step and displayed in a Day plot (Day et al., 1977; Egli, 2021) for each specimen, thus allowing to monitor remanence carrier changes throughout the heating process.

3.2. Paleomagnetism

Paleomagnetic experiments were conducted to determine a mean paleomagnetic direction per oriented site (LPS01 to LPS12). The natural remanent magnetization (NRM) of a total of 108 specimens, 9 per site, was stepwise demagnetized thermally (TH) or by alternating fields (AF). TH demagnetizations were performed on seven specimens per site, using a TD48-SC (ASC) thermal demagnetizer and a 2G SQUID magnetometer at the UBU, with steps from room temperature up to 520–660°C. AF demagnetizations, applied to two specimens per site up to 120 mT, were carried out at the CENIEH research center using a 2G SQUID magnetometer with a three-coil system. Characteristic remanent magnetization (ChRM) directions were determined using principal component analysis (Kirschvink, 1980) in Remasoft (Chadima & Hrouda, 2006), and site-mean directions were calculated hierarchically with PMagTools (Hounslow, 2006).

3.3. Paleointensity

Paleointensity experiments were conducted on samples from all sites using different methods to compare reproducibility: Thellier-Coe (hereafter Thellier), Thellier-Coe with Low Temperature Demagnetization pre-treatment (LTD-Thellier), and Tsunakawa-Shaw involving double heating and LTD pre-treatment (TS). Thellier and LTD-Thellier were performed at the UBU, and TS at MaCRI.

The Thellier method (Coe, 1967; Thellier & Thellier, 1959) was applied to six specimens per site (78 total), which were prepared by drilling ∼8 mm diameter microcores marked for orientation. Double heating steps (zero-field/in-field) were applied progressively up to 520–640°C in an Argon insulated chamber, holding the temperature for 10 min and using fan-assisted cooling, applying 40 μT for the in-field steps. The sequence included pTRM checks at every two temperature steps starting from 300°C. All measurements were performed using a 2G SQUID magnetometer and a TD48-SC (ASC) thermal demagnetizer. Data were processed with ThellierTool 4.2 (Leonhardt & Krása, Krása, 2004) using selection criteria proposed by Paterson et al. (2014) (Table 1).

Table 1
Selection Criteria for Paleointensity Determinations, Where N: Number of Successive Measurement Steps Used for Paleointensity Determination; f: Fraction of Natural Remanent Magnetization Used; q: Quality Factor (Coe, 1978); β: Ratio Between Standard Error and Absolute Slope of the Fit Line; δ (CK): Difference Between the pTRM Check and Original TRM Value at a Given Temperature, Normalized to the TRM (Leonhardt et al., 2004); α(°): Angular Difference Between Vector Average of the Data Selected for Paleointensity Determination and the Principal Component of the Data; MAD (°): Mean Angular Deviation of NRM; f_N: Fraction Used for the Best Fit Line on the NRM-TRM1 plot; r_N: Correlation Coefficient for the Best Fit Line on the NRM-TRM1* Plot; k'_N: Curvature Parameter of the NRM-TRM1* Plot; $Slope_T$: Slope of TRM1-TRM2* of the Second Heating; f_T: Fraction Used for the Best Fit Line on the TRM1-TRM2* of the Second Heating; r_T: Correlation Coefficient for the Best Fit Line on the TRM1-TRM2* of the Second Heating; k'_T: Curvature Parameter of the TRM1-TRM2* Plot*

Selection criteria for thellier-coe (thellier and LTD-Thellier) paleointensity determinations							
Class	N	f	q	β	δ (CK)	α (°)	MAD (°)
Thresholds A	≥5	≥0.35	≥5	≤0.1	≤7	≤15	≤6
Thresholds B	≥5	≥0.35	≥0	≤0.15	≤9	≤15	≤15
Selection criteria for LTD-DHT paleointensity determinations							
Class	f_N	r_N	k'_N	$Slope_T$	f_T	r_T	k'_T
A	≥0.15	≥0.995	≤0.2	0.95–1.05	≥0.15	≥0.995	≤0.2

The LTD-Thellier method was performed on 1–8 specimens per site (57 in total), depending on prior Thellier results. The protocol was identical to the Thellier method but included an LTD treatment after each heating step and before each measurement. LTD was applied by submerging the specimens in a dewar filled with liquid Nitrogen (−196°C) for 2 min and then warmed up until room temperature was reached, all of it inside a shielded device. This pretreatment aimed to remove the contribution of multidomain (MD)-like remanences (Yamamoto et al., 2003). The results obtained were processed identically as in the Thellier method.

The TS method was applied to 2 specimens per site (26 in total), following the procedure detailed in Yamamoto and Tsunakawa (2005) and Yamamoto et al. (2015). It included six progressive AF demagnetizations (up to 180 mT), using a DSPIN spinner magnetometer coupled with an AF demagnetizer (Natsuhara Giken); three anhysteretic remanent magnetizations (ARM), applied approximately parallel to the main ChRM direction after each demagnetization step for correction, with a 50 μT bias field and 180 mT AF peak, and; two TRM acquisitions in vacuum (TRM1: 10 min, TRM2: 20 min). For one set of specimens (one specimen per site), TRMs (TRM1 and TRM2) were applied at 610°C, ensuring the acquisition of a full laboratory TRM. For the second set of specimens (one specimen per site), TRMs were applied at 560°C to assess effects of possible thermal alterations during the process. TRMs of 610°C were applied in both sets on samples from site 12, due to their higher Curie temperatures. All TRMs applied a field of 40 μT in a vacuum jacket, which was subsequently cooled down with a fan. LTD pretreatments were also included before each AF-progressive demagnetization. The results were analyzed with Yamamoto et al.'s (2022) code in PmagPy software (Tauxe et al., 2016), using Kitahara et al.'s (2018) criteria, in addition to k'_N and k'_T criteria (Calvo-Rathert et al., 2024) (Table 1).

4. Results

4.1. Magnetic Mineralogy

Field-emission scanning electron microscope analyses of representative samples exhibited the presence of several ferromagnetic minerals, likely remanence carriers. Opaque mineral abundance ranges from 1.5% in sample LPS12% to 7% in sample LPS06 (Table S2 in Supporting Information S1), with homogeneous distribution throughout the thin sections. The opaque grains show a polymodal grain-size distribution, mostly ≤15 μm, with only a few reaching noticeably larger sizes (Figure 2a). Samples LPS10 and LPS07 stand out for their particularly fine-grained opaques (<10 μm). Textural and mineralogical features of the samples, as well as elemental proportion, provided a valuable insight into the magma crystallization sequence. Most samples displayed stoichiometric magnetites and titanomagnetites (mainly TM20 and TM60). Minor amounts of pyrrhotite were observed in samples LPS09, LPS11, LPS08, and LPS06, typically present as globules smaller than 10 μm, interpreted as primary iron–sulfur (–oxygen) melts trapped in rapidly cooled basalts (Craig & Vaughan, 1994). LPS10 and LPS06 contain grains with chromite cores (Figure 2a), indicative of early crystallization, surrounded

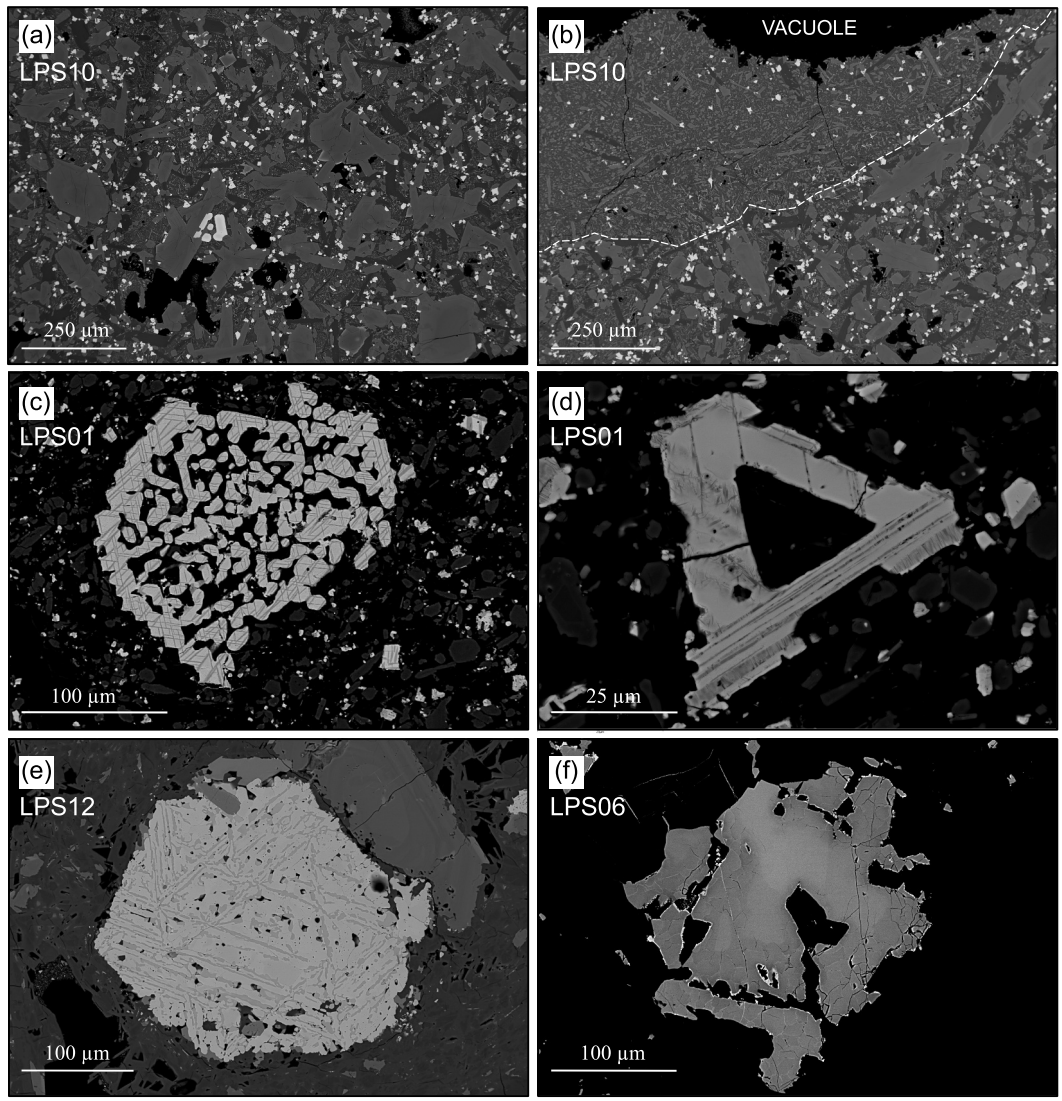

Figure 2. Field-emission scanning electron microscope detail images of different representative samples. (a) General view of the distribution of opaque minerals in sample LPS10: the larger crystals in the central area display darker chromite (Chr) cores surrounded by brighter titanomagnetite rims. (b) Detail of sample LPS10 with two crystallization stages of the magma: in the upper part, a zone depleted in opaque minerals is observed, with smaller crystals. (c) Skeletal titanomagnetite crystal with Trellis-type exsolved ilmenite lamellae in sample LPS12, an example of high-temperature oxidation stage C3 (Haggerty, 1976). (d) Skeletal opaque crystal from sample LPS01: the ilmenite lamellae have transformed into alternating sigmoidal lenses of rutile and titanohematite, characteristic of C4 oxidation stage. (e) Euhedral crystal pseudomorphed to hematite (host phase) with exsolved lamellae of pseudobrookite in sample LPS12, corresponding to stage C7. (f) Skeletal opaque crystal from sample LPS06: thin, curved cracks related to volume changes, along with progressively darker crystal edges due to iron depletion, indicating intense low temperature oxidation.

by titanomagnetite rims resulting from the reaction of the chromite with a Fe-Ti-enriched melt (Haggerty, 1976). In LPS10, successive crystallization stages of the magma are evidenced by a vacuole partially filled with a late-stage melt and rapidly crystallized (Figure 2b). This interpretation is supported by the abundance of fine-grained opaque phases with cruciform and skeletal textures, along with the small size of silicates.

In addition to their primary crystallization features, many of the opaque minerals exhibit textures indicative of oxidation processes. Samples LPS07, LPS01, LPS12, and LPS06 show clear evidence of high-temperature oxidation. According to their mineralogical features and the oxidation stages defined by Haggerty (1976, 1991), the degree of oxidation ranges from stage C2 to C7 (Table S2 in Supporting Information S1). Early to intermediate stages (LPS06 and LPS01), are marked by the presence of Trellis-type ilmenite lamellae within

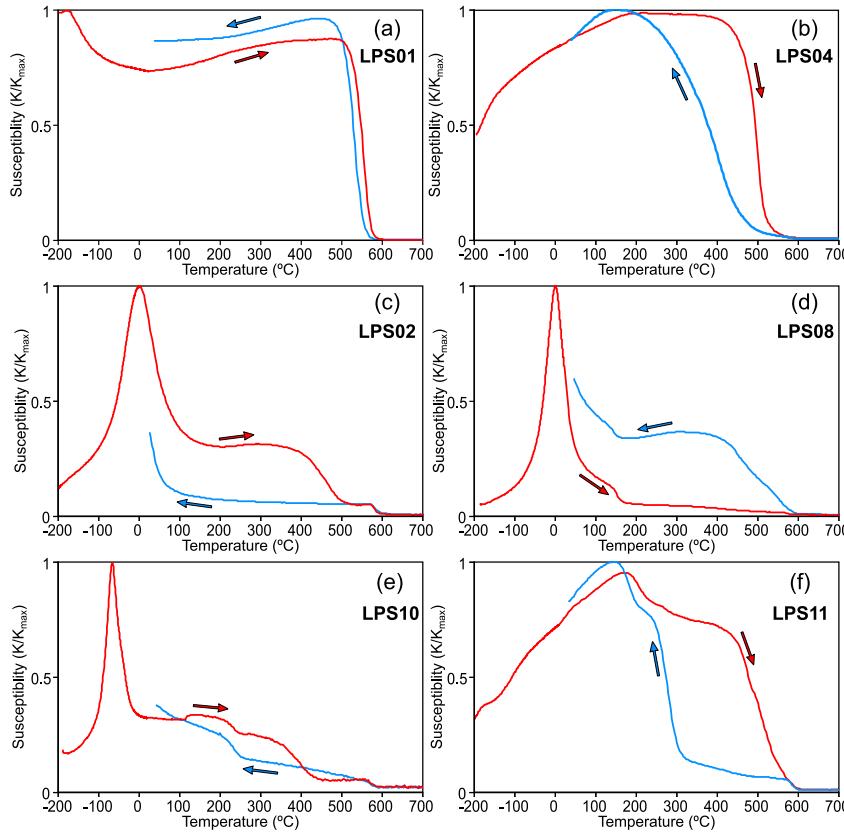

Figure 3. Susceptibility versus temperature curves of representative samples: (a) sample from LPS01; (b) sample from LPS04; (c) sample from LPS02; (d) sample from LPS08; (e) sample from LPS10; (f) sample from LPS11.

titanomagnetite crystals (Figure 2c). In more advanced stages (LPS01), these lamellae evolve into alternating lenses of rutile and titanohematite (Figure 2d). In the most oxidized samples, LPS07 and LPS12, the mineral assemblage transforms into pseudobrookite plus hematite, with pseudobrookite replacing former ilmenite lamellae and hematite substituting titanomagnetite (Figure 2e). Maghemite, indicative of low-temperature oxidation, was identified in only two samples through optical analyses: LPS11 and LPS06. Notably, LPS06 is the only case exhibiting features of both high- and low-temperature oxidation. In this specimen, ilmenite exsolution lamellae are confined to a few larger crystals, whereas many of the opaque phases display textures, such as irregular cracks, indicative of low-temperature oxidation (Figure 2f).

Variable Field Translation Balance experiments yielded rather homogeneous results (Figure S1 in Supporting Information S1). Magnetization versus temperature curves indicate Curie temperatures of magnetite (560–580°C), with some samples showing intermediate temperature phases linked with highly substituted Ti-magnetites or Ti-maghemites. Curves with intermediate phases typically display partial or total transformation into magnetite during the heating. In all cases, hysteresis loops exhibited pot-bellied shape, and IRM curves reached saturation at low fields (200–300 mT).

Susceptibility versus temperature experiments allowed distinguishing a wide variety of behaviors, which have been classified into six types illustrated in Figures 3a–3f. Type a, observed in samples LPS01, LPS09, LPS07 and LPS12, resembles MD-like magnetite shape (Dunlop, 2014) with a Verwey transition around −130°C and being mainly reversible. The latter two samples include intermediate temperature phases as well. Type b, (LPS04 and LPS13), shows a single susceptibility drop at ∼530°C, likely linked to low Ti-substituted magnetite (TM20) (Muxworthy et al., 2023); the Verwey transition can also be observed, although slightly hidden by the increase of the susceptibility with temperature, proving a very similar composition to the previous type but probably with finer grain size, in addition, the decrease of magnetization in the cooling branch is consistent with cation rearrangements of poor-substituted TM during the heating (Jackson & Bowles, 2018). Type c, (LPS02 and LPS06),

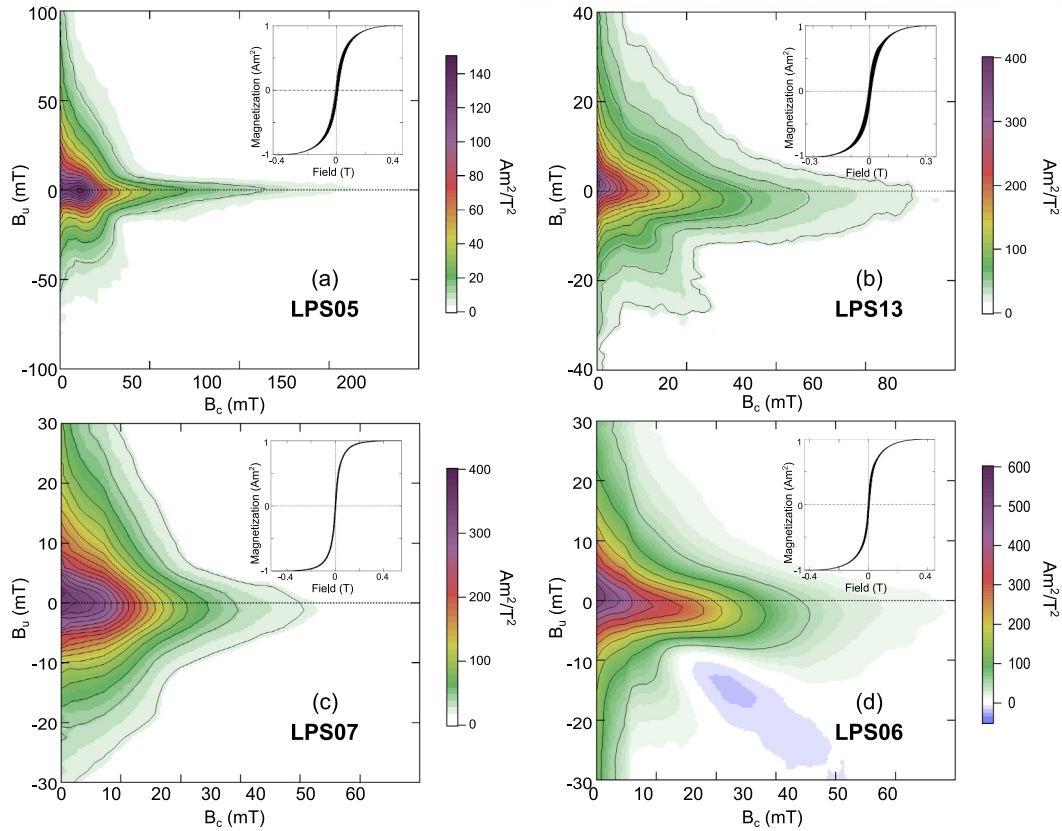

Figure 4. First Order Reversal Curves plots and their hysteresis loops of representative samples with different behaviors: (a) sample from LPS05; (b) Sample from LPS13; (c) sample from LPS07; (d) sample from LPS06.

has a sharp Hopkinson peak, which varies between samples from −100°C to room temperature, indicating highly Ti-substituted magnetite as TM60 (Muxworthy et al., 2023). It also displays a susceptibility "hump" between intermediate temperatures (150°C to 400°C), which disappears after heating; characteristic for maghemite (Kontny & Grothaus, 2017), and a drop at the stochiometric magnetite Curie temperature (580°C). Type d, (LPS03, LPS05 and LPS08), displays a Hopkinson peak (at ∼0°C) for highly Ti-substituted magnetite (TM60), and the "hump" observed in the cooling curve could be due to the formation of magnetite or the movement of domain walls of the TM during the heating process (Vahle & Kontny, 2005). Type e, (only in LPS10), has a Hopkinson peak (at −100°C to 0°C) that indicates highly Ti-substituted magnetite (TM80) (Muxworthy et al., 2023); it also displays several inflections at intermediate and high temperatures (∼220°C, ∼410°C and 580°C), the first associated with TM60 or similar, the second with maghemite, which disappears in the cooling branch, and the latter for stoichiometric magnetite. Type f (LPS11), with a Verwey transition and a reversible Curie temperature for probably MD-like stoichiometric magnetite, a Hopkinson peak at temperatures characteristic of TM60 and a non-reversible susceptibility drop at ∼550°C, as well as a similar decrease of magnetization in the cooling branch due to cation reordering (Jackson & Bowles, 2018).

FORCs and their hysteresis loops showing four different behaviors are plotted in Figure 4. LPS05 (Figure 4a) displays an asymmetry of the contours with a typical vortex shape, characteristic of PSD or vortex grains. It has closed contours around low coercivities (∼15 mT) and sharp elongation along B_c, indicating a range of components from low to high coercivities (>100 mT). LPS12 (Figure 4b) displays elongation along B_c with open contours, showing a PSD-vortex shape as well. LPS07 (Figure 4c) shows mostly symmetrical open contours forming a triangular shape, characteristically of MD. LPS06 (Figure 4d) has an elongation around B_u, suggesting low coercivity viscous behavior (MD/SP grains), and elongation along B_c, indicating SD grains contribution (Roberts et al., 2000).

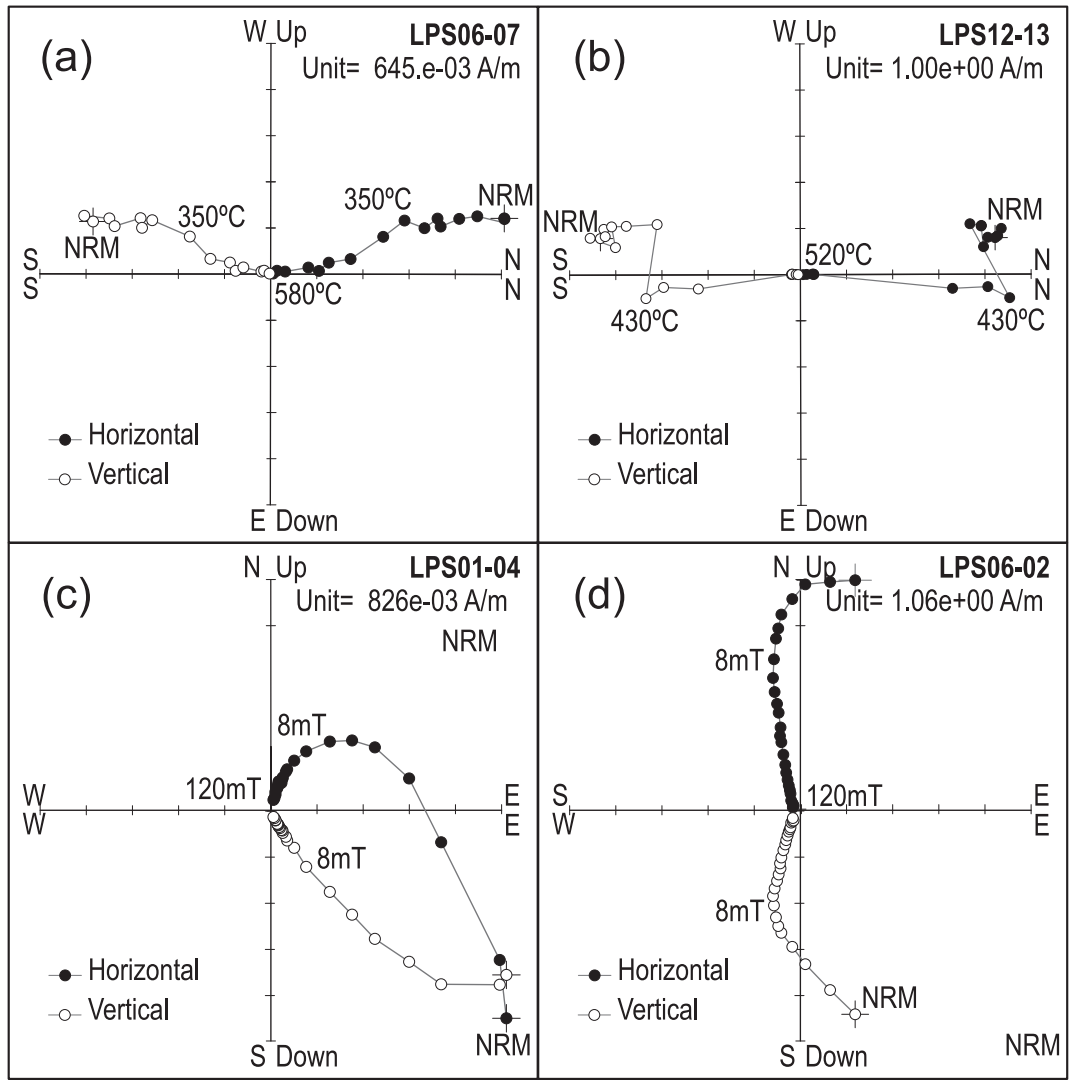

Figure 5. Representative orthogonal natural remanent magnetization demagnetization diagrams of thermal (a, b) and alternating field (c, d) treated specimens. (a) Sample from LPS06; (b) sample from LPS12; (c) sample from LPS01; (d) sample from LPS06.

4.2. Paleomagnetic Directions

Both thermal and alternating field progressive demagnetizations displayed a primary component defined as the ChRM component and, in many cases, a secondary component with different directions within the same lava-flow. The latter component was demagnetized at around 350°C or even higher temperatures applying thermal demagnetization (Figures 5a and 5b) and around 10 mT for AF demagnetization (Figures 5c and 5d). Most of the AF demagnetizations show a partial overlap of this component with the high coercivity component. The low temperature or coercivity component has been associated with a strong viscosity contribution, carrying inconsistent directions. Paleomagnetic directions were calculated from the ChRM component (Table S3 in Supporting Information S1), hierarchically obtaining a mean direction for each oriented site (Table 2).

4.3. Paleointensity Determinations

Paleointensity determinations have been assessed separately by method, calculating a mean value per site and method when possible.

Table 2

*Paleomagnetic and Paleointensity Results (Thellier, LTD-Thellier and TS) per Site Along With Its Locality Name and Absolute Age (Ka BP), Where; Dec (°): Declination; Δ_D: Declination Error at 97.5% (According to Demarest, 1983); Inc (°): Inclination; Δ_I: Inclination Error at 97.5% (According to Demarest, 1983); α_{95} (°): Confidence Limit of the ChRM at 95% Level; n/N: Number of Accepted Specimens Versus Number of Studied Specimens; B: Estimated Absolute Paleointensity Value (in μT); Δ_B: Error Value Associated to the Intensity Estimation (in μT); *: TS Paleointensity Estimations Which Could Result in Biased Results; -: Without Results*

									Paleointensity determinations							
		Paleomagnetic directions							Thellier			LTD-thellier			TS		
Site	Locality	Age (ka BP)	Dec (°)	Δ_D (°)	Inc (°)	Δ_I (°)	α_{95} (°)	n/N	B (μT)	Δ_B (μT)	n/N	B (μT)	Δ_B (μT)	n/N	B (μT)	Δ_B (μT)	n/N
LPS12	Roque Teneguía	56 ± 2	20.5	14.8	36.4	11.9	15.9	3/3	–	–	0/6	46.6	1.7	4/8	–	–	0/2
LPS05	La Fajana - Volcán Fuego	36 ± 1	3.2	8.3	46.8	5.7	7.3	8/9	47.1	3.5	4/6	35.4	4.3	4/4	51.4	0.36	1/2
LPS03	Cliff of Puerto Tigalate	27 ± 1	349.5	7.1	43.4	5.1	6.6	8/9	12.3	3.3	4/6	13.2	4.2	4/5	28.8	4.7	2/2
LPS11	Lava dome of Mendo	26 ± 1	318.4	14.2	36.2	11.5	15.1	4/9	27.4	7.6	2/6	25.0	5.2	2/3	36.9*	0.6	1/2
LPS01	Tiguerorte	25 ± 2	9.4	16.3	44.4	11.6	14.9	7/9	27.1	1.5	1/6	26.0	8.2	3/5	47.5	5.4	2/2
LPS02	Las Salineras	21 ± 2	352.9	8.4	49.4	5.5	6.9	9/9	–	–	0/6	–	–	0/5	–	–	0/2
LPS04	Cliff of Puerto Tigalate (80 m)	20 ± 2	351.4	21.8	53.5	12.9	16.6	6/9	29.8	1.8	2/6	29.8	1.5	1/8	22.6*	0.4	1/2
LPS09	C-832 km 39 km 34	18 ± 2	24.7	5.9	32.8	4.7	6.0	9/9	37.6	6.2	3/6	33.3	2.8	1/2	–	–	0/2
LPS10	Cliff of Playa Nueva	8 ± 2	353.8	9.5	49.1	6.2	7.9	5/9	28.4	1.5	1/6	–	–	0/5	65.6	0.5	1/2
LPS06	Road to airport, km 1.2	8 ± 1	355.1	6.7	36.6	5.4	6.9	6/9	25.3	0.7	1/6	19.3	6.0	3/5	–	–	0/2
LPS08	Las Indias	3 ± 2	0.8	9.1	33.8	7.6	9.7	8/9	–	–	0/6	–	–	0/4	49.6	0.5	1/2
LPS13	La Fajana	3.2 ± 0.01			–				54.4	7.2	6/6	54.3	1.7	2/2	70.5	0.5	1/2
LPS07	Montaña Goteras	1.09 ± 0.05	0.5	8.1	49.3	5.3	6.8	7/9	35.1	3.1	6/6	–	–	0/1	59.5	0.6	1/2

For the Thellier experiments, the numerical selection criteria shown in Table 1 were applied and, additionally, some results were discarded because of the concavity of the Arai plots (Figure S2 and Table S4 in Supporting Information S1). Initially, we calculated curvature parameter *k* (Paterson, 2011) to be used as a numerical criterion to assess the presence of MD gains. However, it should be considered that this parameter can also be affected by factors like alteration besides the presence of MD grains. In the present case, while some moderately concave Arai plots were not identified as such, LTD–Thellier specimens displaying two-segment pattern yielded high *k* values. Because of this ambiguity, we ultimately relied on a visual characterization of the concavity of Arai plots. The observed slight to major curvature in the Arai plots indicates a large influence of MD-like grains in such samples. Other specimens displayed erratic points producing uncoherent Arai plots, resulting in a failure to produce a straight line and suggesting a strong magnetic viscosity (Figure 6a). In addition, many results producing a straight line and plausible paleointensity estimations yielded non-acceptable δ(CK) values. Finally, 38.5% of specimens were accepted (Table 2).

In the case of TS experiments, 12 out of 26 specimens yielded successful results (Table 2; Table S5 and Figure S3 in Supporting Information S1) according to the selection criteria. In addition, results of the specimens from site LPS12 were discarded, because their ChRMs could not be completely demagnetized at 180 mT, as the remanence is mainly carried by hematite, finally resulting in 11 accepted results. The use of different heating temperatures for imparting TRMs (560°C and 610°C) did not yield significant differences in success rates. The main reasons for rejection have been (a) thermal alteration during the experiments, identified through non-unity TRM1/TRM2* ratios, (b) dissimilarity between TRM (NRM) and ARM, identified through larger k'_N and k'_T, and (c) the partial overlapping of the main component and the viscous one, as this method is based on the coercivity spectra (Figure 7b).

Additionally, changes of efficiency between TRM and ARM acquisition in laboratory have been considered based on TRM/ARM ratio, which can be a measure of magnetic grain size (Dunlop & Argyle, 1997). Since ARMs (ARM0, ARM1 and ARM2) and TRMs (TRM1 and TRM2) were respectively imparted under the same laboratory conditions, if no significant change occurred during the second laboratory heating, TRM1/ARM1 (R_1) and TRM2/ARM2 (R_2) ratios should remain similar. The inconsistency of R_1 and R_2 ratios has been suggested to be a

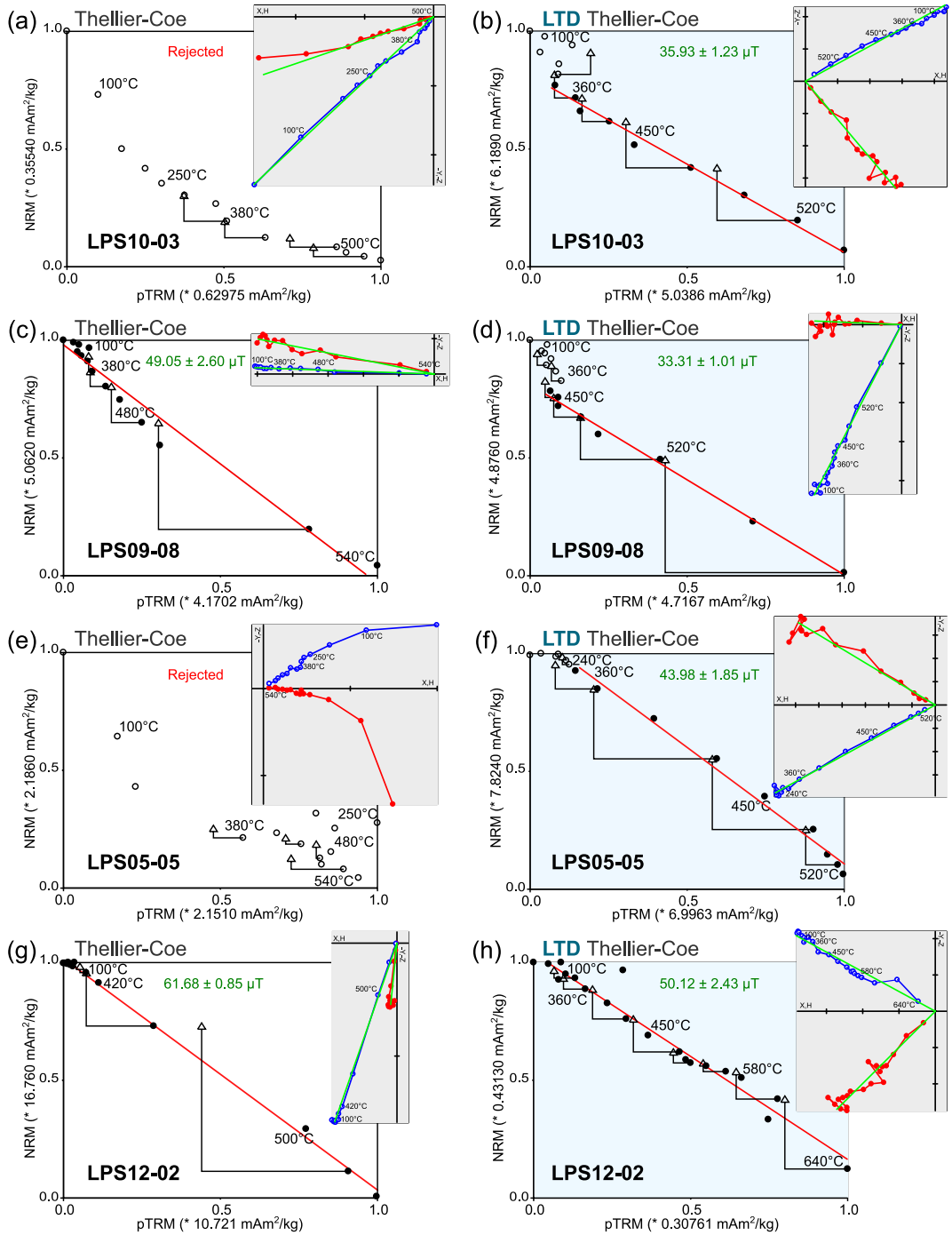

Figure 6. Comparison of Arai plots obtained through Thellier-Coe experiments without LTD pretreatment on the left (a, c, e, and g) and with LTD pretreatment on the right, denoted in blue, (b, d, f, and h), with their correspondign Zijderveld plots. Set of four representative sister specimens: (a, b) specimen LPS10-03; (c, d) specimen LPS09-08; (e, f) specimen LPS05-05; (g, h) specimen LPS12-02.

cause of possible biased paleointensities, indicating changes in magnetic grain sizes promoted by thermal alteration (Qi et al., 2024). Only 2 of the accepted specimens displayed R_2/R_1 differences above 10% and have been noted as possible biased results (Table 2; Figure 9a). The ARM correction allowed obtaining a straight line in several cases (Figure 7a; see also Figure S3 in Supporting Information S1) while the LTD pretreatment likely

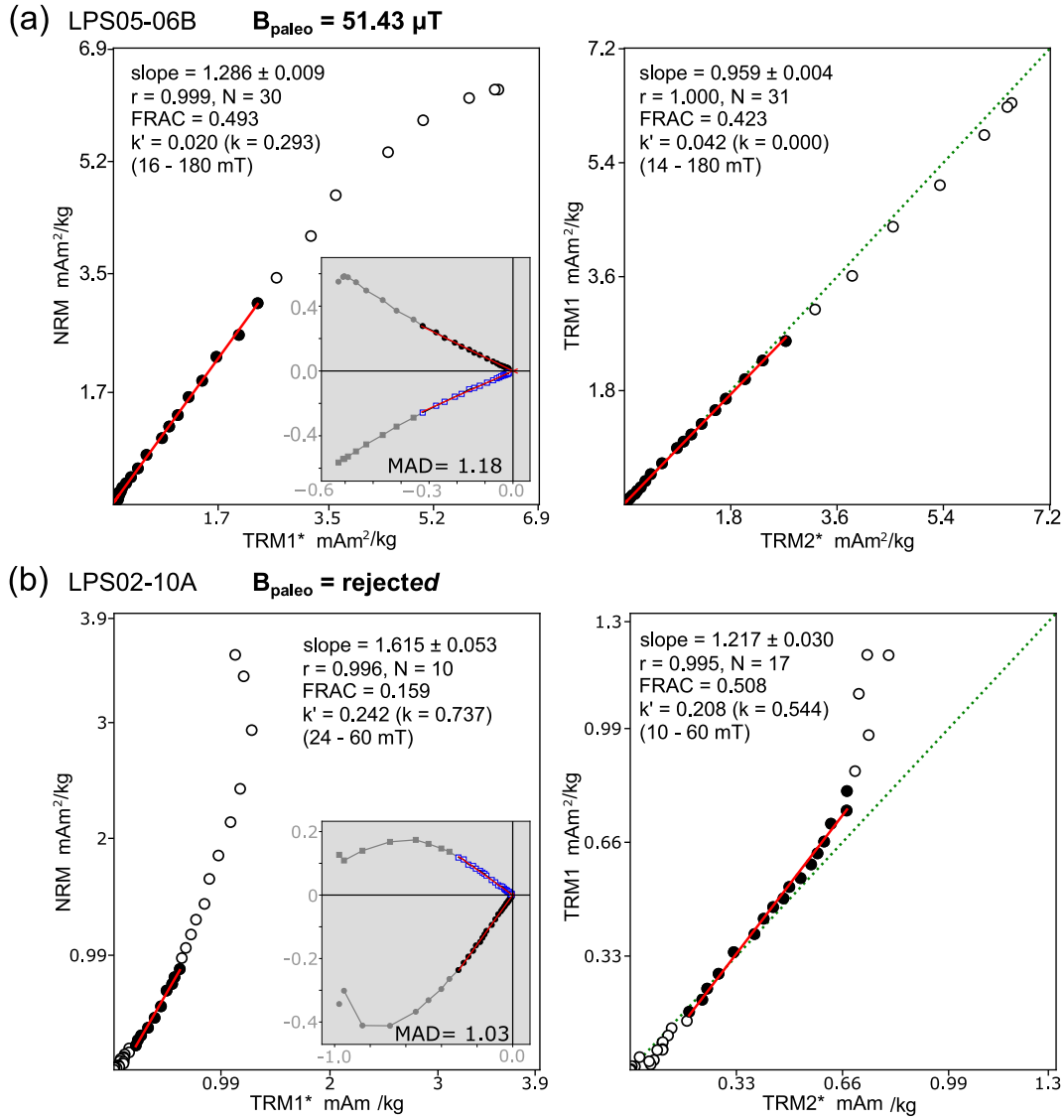

Figure 7. Tsunakawa-Shaw paleointensity results for two representative samples. Arai plot with natural remanent magnetization (NRM) versus TRM1* on the left and the NRM demagnetization plot inside in gray, TRM1 versus TRM2 on the right, (a) is representative of a successful specimen and (b) is representative of a failed specimen.

contributed by removing viscous overprints. Consequently, the highest success rate in this study was obtained through TS the method (42.3%).

To avoid the overlap of components with partially similar coercivities and the thermal alteration of a full TRM, while still benefiting from demagnetization of non-ideal SD grains through LTD, a Thellier-Coe method including LTD pretreatment was performed. The strong viscous component and ChRM could be better differentiated than by coercivity spectra, and moreover, being based on partial TRMs, better control of thermal alterations was achieved. For this method, sister specimens of those previously studied using standard Thellier were selected, chosen among those displaying a certain concavity. Despite that, the LTD-Thellier method achieved a higher success rate (42.1% vs. 38.5%). One specimen of this set (LPS0901) was discarded because of its higher paleointensity value in comparison with the specimens from the same site. It was sampled in the uppermost part of the lava-flow LPS09 and could have been thermally affected by the emplacement of the lava-flow lying above.

The Arai plots obtained with the LTD-Thellier method deserve a closer look as different effects could be observed. Figure 6 shows four representative examples, comparing Arai plots obtained for sister specimens with

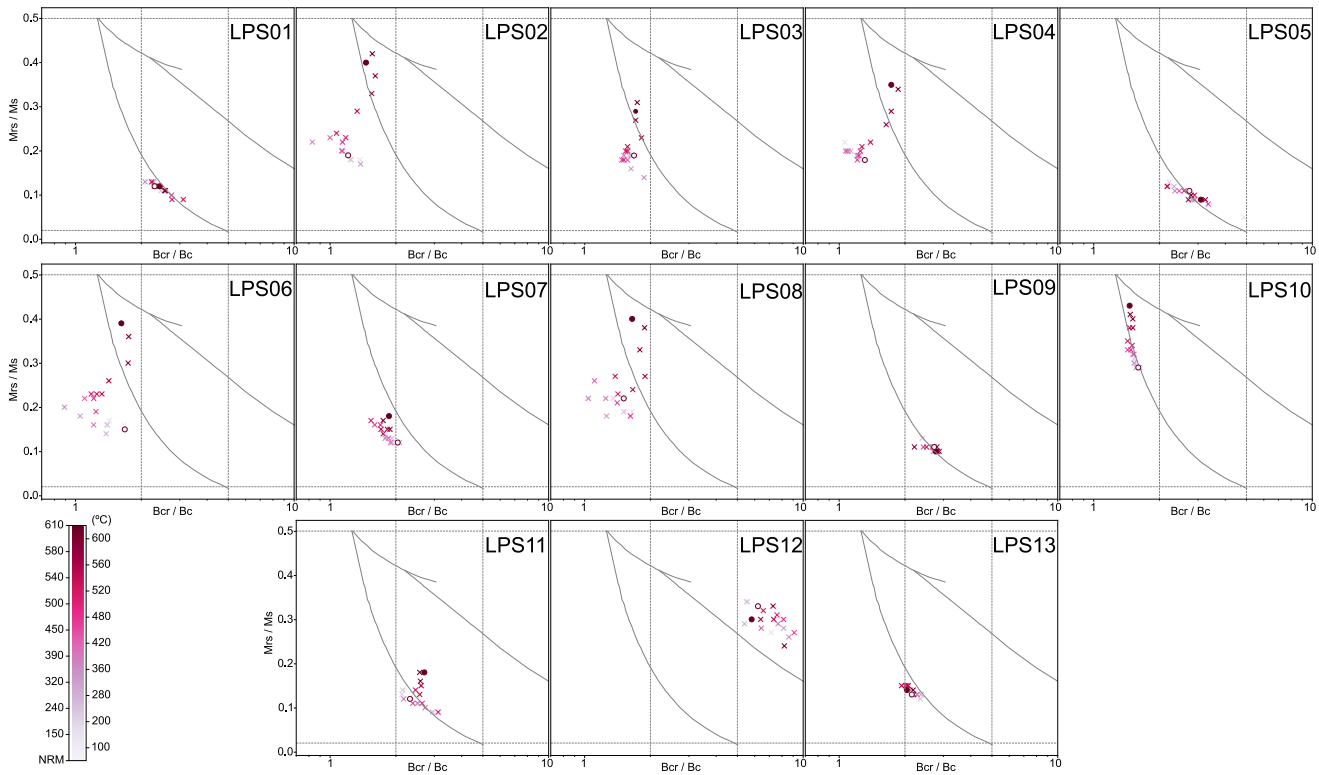

Figure 8. Day plots (Day et al., 1977; Egli, 2021) for a representative sample from each site after applying different heating steps used during paleointensity experiments. Data in Table S6 of Supporting Information S1.

the Thellier and LTD-Thellier methods. Further representative examples are in Figure S2 in Supporting Information S1. In Case 1 (Figures 6a and 6b), the Arai plot without LTD exhibits a pronounced MD-type concavity that precludes extracting a robust linear trend for paleointensity calculation (a). When LTDs are applied (b), the concavity disappears, separating two segments; the first one, at low to intermediate temperatures, which represents a variable amount of the total NRM -reaching 50% in some cases-, basically does not acquire any TRM in laboratory. The high temperature component, associated with the primary TRM, displays well-aligned points suitable for paleointensity estimations. In Case 2 (Figures 6c and 6d), as in Case 1, the Arai plot of the non-treated specimen (c) is slightly curved, mild enough to pass the standard selection criteria. When LTD pretreatments are applied (d), two different components are also distinguished. The high temperature component is less steep than without LTD pretreatment, which leads to obtaining a lower paleointensity determination with LTD-Thellier. This example proves that paleointensity determinations with classical protocols without pretreatments can be easily overestimated because of the overlap of a low temperature viscous-like component in the Arai plot slope. In Case 3 (Figures 6e and 6f), the specimen without LTD pretreatment (e) displays a very weak magnetization with incoherent points along the Arai plot. When the LTD pretreatment is applied (f), the demagnetization of the magnetic viscosity reduces the viscous overprint and thereby increases the relative contribution of the primary magnetic component, allowing to visualize a straight slope suitable for paleointensity estimations. Case 4 (Figures 6g and 6h) is analogous to Case 3, although it is more critical. While the untreated specimen (*g*) already displays a suitable slope for paleointensity determinations, the LTD treated sample (h) displays a higher blocking temperature interval. This phenomenon changes dramatically the resulting paleointensity estimation, showing that the non-LTD treated sample again overestimates the paleointensity determination. As in Case 3, LTD demagnetization reduces low blocking temperature viscous components, making the high blocking temperature component more visible and allowing a paleointensity value to be calculated from the magnetically "harder" grains. It is worth noting that Case 4 occurs only in specimens from site LPS12, which has a distinctly different mineralogical composition compared to the other lava-flows, mainly characterized by the presence of hematite, whose contribution remains hidden in non-LTD treated specimens.

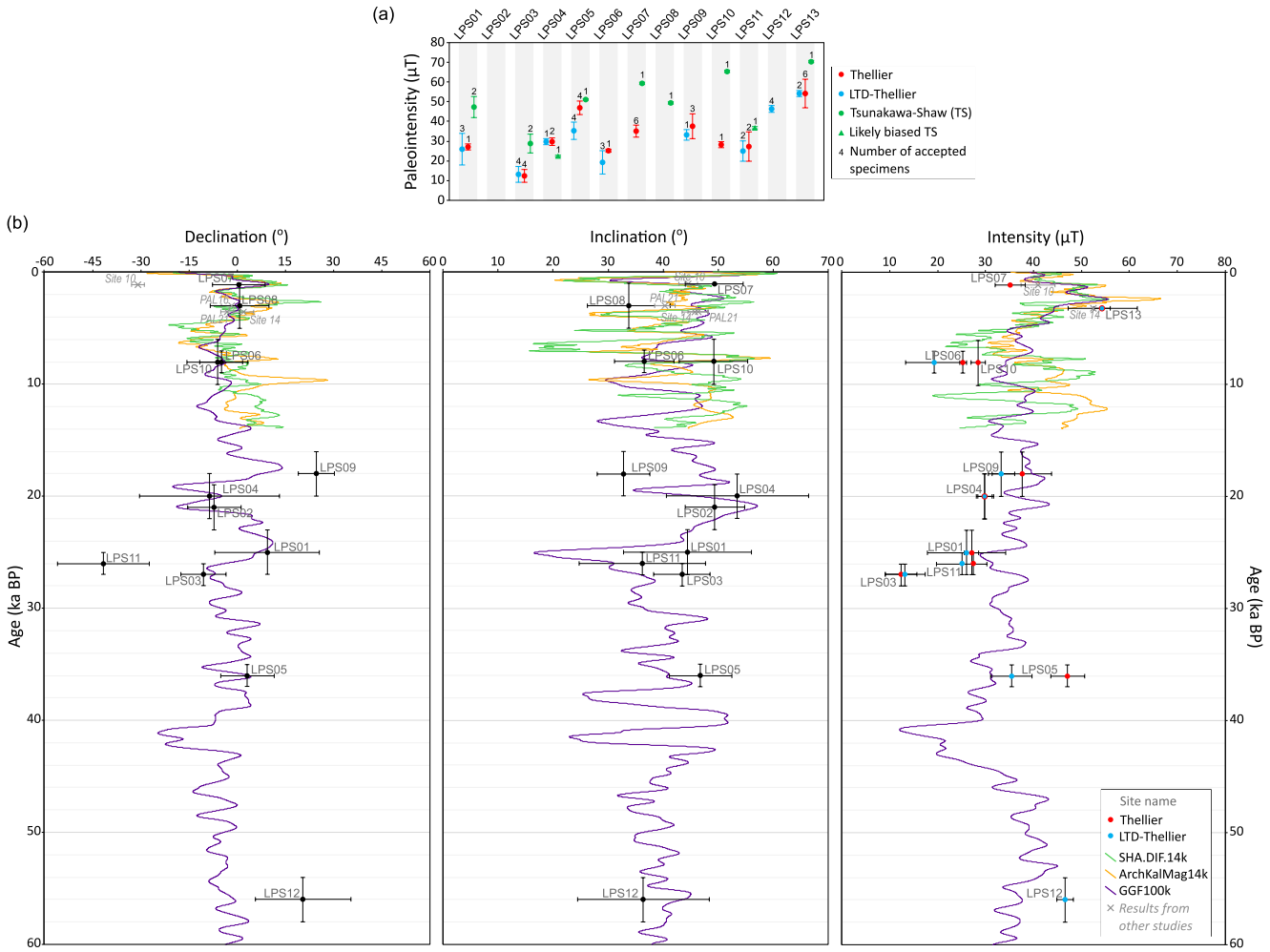

Figure 9. (a) Paleointensity mean estimations plotted per site and method (Thellier, LTD-Thellier and TS), mean values in Table 1. (b) Results of declination, inclination and field intensity per site and age obtained from this study, compared with the paleosecular variation curves obtained at La Palma coordinates from the global models of SHA.DIF.14k (Pavón-Carrasco et al., 2014), ArchKalMag14k (Schanner et al., 2022) and GGF100k (Panovska et al., 2018). Results from other studies in La Palma lava flows; Site 10 and Site 14: Monster et al. (2015); PAL16 and PAL21: Magli et al. (2025).

Finally, to prove whether the frequent low coherency of the pTRM-checks was produced because of thermal alteration or the contribution of MD grains (Jeong et al., 2021), the B_{cr}/B_c and M_{rs}/M_s ratios at different temperature steps were calculated (Figure 8; Table S6 in Supporting Information S1). These experiments show, on the one hand, that the magnetic domain state of the specimens appears in most cases along the mixing curve of single-domain and multi-domain to pseudo single-domain (SD + MD, PSD), with high contribution of MD, although the high values of B_{cr}/B_c typical for solely MD domains are not reached. The only exception is sample LPS12, for which all data points fall along the superparamagnetic and single-domain (SP + SD) mixing line. However, its magnetic mineralogy dominated by hematite may affect the position on this plot, which is primarily based on magnetite characteristics. On the other hand, below 540°C domain states remain practically unchanged, pointing toward negligible heating alteration below that temperature during the paleointensity experiments. In specimens from sites LPS02, LPS03, LPS04, LPS06, LPS08, LPS10 and LPS11, which display higher alteration above that temperature, M_{rs}/M_s ratios move toward higher values with increasing the temperature and, perhaps, slightly higher B_{cr}/B_c ratio values as well. The increase of these ratios aligns with a maghemitization process (Almeida et al., 2015; Muxworthy, 1999), therefore suggesting that oxidation promoted by heating occurs during paleointensity experiments, but it has been considered only significant above 540°C. This experiment suggests that the failure of pTRM-checks, mainly below 540°C, with their expected value might be caused by the presence of MD-like grains rather than by a thermal alteration.

5. Discussion

5.1. Magnetic Mineralogy of Viscous Remanence Carriers

Strong viscous components consistently observed in this study posed significant challenges to paleointensity estimations, as observed in the most recently erupted La Palma lava-flows (Calvo-Rathert et al., 2024). This behavior, linked to domain state and alteration processes, affected the stability of the remanent magnetization (Larson et al., 1969), resulting in magnetic viscosity with anomalously high unblocking temperatures inconsistent with those expected in geologically recent lava-flows (Pullaiah et al., 1975). Low-temperature oxidation or maghemitization features, and irreversible rearrangement of the domain state of PSD-vortex grains have been reported to produce such high unblocking temperatures (Jackson & Worm, 2001; Tanaka & Yamamoto, 2016). In this study, we have attempted to unveil the composition and contribution of such viscosity.

On the one hand, high-temperature oxidation at advanced stages (C3 to C7), observed through FE-SEM in sites LPS01, LPS07 and LPS12 (Table S2 in Supporting Information S1), appears to correlate with thermal stability (Figure 8), reversible thermomagnetic behaviors and high success rates in paleointensity estimations (Table S7 in Supporting Information S1). Nevertheless, the main reason for rejection of Thellier estimations of these specimens was failure of pTRM-checks (Table S4 in Supporting Information S1), at least partially caused by MD-grains contribution. This fact is supported by the MD-like susceptibility curves (Figure 3a), triangular-shaped FORCs (Figure 4c) and Day plots (Figure 8) that these samples display.

Conversely, low-temperature oxidation (or maghemitization) was linked to reduced paleointensity reliability and lower success rates (Table S7 in Supporting Information S1). Maghemitization produces vacancies and cation reordering in the crystalline structure of titanomagnetites, leading to the replacement of the original TRM by a thermo-chemical magnetic remanence (TCRM) and increasing the stability of viscosity carriers (Wang et al., 2021). Although FE-SEM only revealed the presence of low temperature oxidation in two samples (Table S2 in Supporting Information S1: LPS11 and LPS06), magnetization and susceptibility curves allowed determining maghemite in several cases (LPS02, LPS06, LPS10, LPS11), in the case of the susceptibility curves, by the observation of a characteristic "hump" between intermediate temperatures (150°C-400°C), which disappears after heating (Figures 3c and 3e). According to susceptibility curves, samples from sites LPS06 and LPS02 (Figure 3c) display a large contribution of maghemite, which has been linked to their incoherent paleointensity results, displaying viscous behavior or concave Arai plots (Figure S2, Table S4 in Supporting Information S1). In addition, all samples containing maghemite display irreversible magnetization versus temperature curves and show some thermal alteration above 540°C (Table S7 in Supporting Information S1).

Sites LPS13 and LPS04, apparently unaffected by any oxidation processes and containing low Ti-substituted magnetite phases (Figure 3b) and PSD-vortex rather than MD-grains (Figure 4b), displayed higher success rates and a relatively good agreement among the different paleointensity methods. By contrast, the successive crystallization stages observed in samples from site LPS10 though FE-SEM could have led to their particular susceptibility behavior (Figure 3e): samples from this site display thermal irreversibility as well as low success rates due to typically MD-concave Arai plots.

5.2. Consistency of Paleointensity Determinations Among Different Methods

Among the techniques applied, the Thellier experiments exhibited the lowest success rate, despite preselecting specimens based on their rock-magnetic and thermal behaviors. Failures were attributed to: (a) concavity in the Arai plots, (b) erratic data points in a few cases, and (c) high, unacceptable δ(CK) values despite otherwise acceptable behavior (Figure S2 and Table S4 in Supporting Information S1).

The TS method mitigated the influence of non-SD components through ARM correction, DHT criteria, and LTD pretreatment (Tauxe et al., 2021). Of the 11 accepted paleointensity results, 9 correspond to different sites (Table 2; Table S5 in Supporting Information S1). Due to low thermal conductivity within the vacuum jacket, actual specimen temperatures may be ∼10–20°C lower than the set point. Thus, heating is typically conducted at 610°C, appropriately above the Curie temperature of stoichiometric magnetite (TM0), to ensure full TRM acquisition. It is noteworthy to mention that similar success rates have been obtained for samples treated at different TRM temperatures. However, given the small number of paleointensity estimates per site, the overall picture is unclear, and no stringent conclusions can be obtained. Nevertheless, it is emphasized that LTD pretreatment plays a critical role in suppressing viscous overprints.

LTD integration into the Thellier protocol addressed MD-related artifacts in many cases. For the case of failure (a) described above, it successfully reduced concavity revealing a two-segment pattern (Figures 6a–6d); a low-to intermediate-temperature segment, characterized by a very low acquisition of magnetization and associated with the viscous component, and a high temperature segment reflecting the original TRM. It also magnified the paleointensity signal carried by SD-grains, thus achieving neater Arai diagrams and addressing issue (b) (Figures 6e–6h). In both cases, the Arai plot of non-LTD treated Thellier merges the viscous (TCRM) with the TRM components, resulting in a steeper slope and in paleointensity overestimation. This proves that undetected viscosities can be easily a source of bias in paleointensity estimations.

The effect of alignment in the Arai plots of samples treated by LTD-Thellier has been already reported in previous studies (e.g., Yamamoto et al., 2003; Smirnov et al., 2017). Concavity in Arai plots, usually associated with MD-like grains, may also stem from low temperature oxidation, due to inequality between blocking and unblocking temperature spectra associated with the remanent magnetization controlled by magnetocrystalline anisotropy (Yamamoto et al., 2022). This concavity can also be aggravated by aging, due to the likely increase of such non-ideal remanence carriers over time (Tauxe et al., 2021). The magnetocrystalline anisotropy constants of Ti-poor titanomagnetites approach zero at temperatures between −130°C and −180°C (Syono & Ishikawa, 1963), allowing to remove their remanence by applying LTD with liquid Nitrogen in zero field. In fact, all studies using the LTD-Thellier method have reported higher success rates in comparison with the classic method. Nevertheless, LTD demagnetization might be inefficient with severe oxidation (Smirnov et al., 2017). Although AF demagnetization at 10 mT has been proposed as an alternative (Dunlop & Özdemir, 2001), it has proven ineffective in certain cases where LTD succeeded (Yamamoto et al., 2022), highlighting LTD's broader applicability in isolating and enhancing the primary remanence.

Bias in paleointensity estimates arising from non-ideal carriers has been extensively discussed (e.g., Yamamoto et al., 2003, 2022; Tanaka & Komuro, 2009). A historical Hawaiian lava-flow study (Yamamoto et al., 2003) showed the similar two-segment pattern described here. In that case, erroneous estimations were linked to changes in the structure of PSD-like grains, fostered by low temperature oxidation. Non-ideal carriers and TCRM acquired during low temperature oxidation can therefore be a source of erroneous paleointensity estimations despite passing strict selection criteria, whereas the actual paleointensity might remain hidden.

Regarding the cause of failure (c), the frequent rejection of results due to pTRM-checks was assessed with thermal alteration experiments. These indicated no or very mild alteration below 540°C during the paleointensity experiments. In fact, pTRM-checks can be affected by both thermal alterations and Arai plot concavity, thus, not being always a reliable indicator of alteration (Wang & Kent, 2013). Here, MD-like grains likely led to most of the negative pTRM-checks. Many reliable results were discarded due to unacceptable δ(CK) values, which proved an unreliable thermal alteration proxy. Positive pTRM-checks cannot completely exclude failed results (Jeong et al., 2021), as proven by studies where known field intensities were not recovered despite passing checks (e.g., Cromwell et al., 2015; Yamamoto et al., 2003). Even with a noticeable improvement obtained through LTD-Thellier, high δ(CK) values remained a common cause of failure, suggesting significant MD-grains presence and/or severe low temperature oxidations unremovable by LTD (Smirnov et al., 2017).

Paleointensity estimates obtained using different methods exhibited notable characteristics depending on the method (Table 2; Figure 9a). While LTD-Thellier results occasionally agreed with standard Thellier method, they generally yielded lower paleointensity values. Previous studies have reported underestimations in Thellier-based paleointensity measurements for samples affected by TCRM (e.g., Qin et al., 2011; Smirnov & Tarduno, 2005). Conversely, overestimations due to overlapping viscous and TRM components, as those observed here, have been noted by Yamamoto (2006). In this study, overestimation in non-LTD-treated Thellier specimens ranged from 0% to 30%. In addition, the TS method consistently yielded higher paleointensity estimations than Thellier-type methods, except for sites LPS04, which displays lower values through TS, and LPS08, for which no comparison was possible. However, as stated previously, the small number of TS-accepted estimations inhibit a thorough evaluation about this poor coherency.

5.3. Paleosecular Variation in La Palma Over the Last Millennia

Figure 9b shows the variation of declination, inclination and intensity versus time (56–1 ka) obtained in the present study, compared with the PSV curves GGF100k (Panovska et al., 2018) for the past 100 ka and

ArchKalMag14k (Schanner et al., 2022); SHA.DIF.14k (Pavón-Carrasco et al., 2014) for the past 14 ka, all calculated at La Palma coordinates.

Directional (declination and inclination) values are mostly consistent with all three PSV curves, especially for the younger lava-flows. Outlier values have been obtained for sites LPS09, LPS11 and LPS12. Because of their age, these sites could be only compared with the GGF100k model, which is based on sedimentary data and could result in smoothed curves. Nevertheless, the low declination of LPS11 remains unusual, despite its large scatter. Magli et al. (2025) present paleomagnetic dating for several lava-flows in La Palma based on directional data which includes two sites from the present study (LPS13 and LPS08). Paleomagnetic results of the latter site (PAL16 in Magli et al., 2025) agree with our study (Figure 9b), but the paleomagnetic direction of the unoriented site LPS13 (PAL21 in Magli et al., 2025) could not be compared.

For the reasons explained previously, only paleointensity estimations obtained through Thellier-type methods, preferably LTD-Thellier, were considered in this section, to avoid possible overestimations. The paleointensity estimation of site LPS07 through Thellier is consistent with the expected field intensity curves, and in good agreement with the paleointensity determination obtained by Monster et al. (2015) for the same lava-flow through the Microwave method (Site 10 in that study), within its uncertainty (Figure 9b). The relatively high paleointensity values of LPS13 (~54 μT, VADM ~108 ZAm^2), with a good agreement between the two Thellier-type methods, are chronologically compatible with the initial stage of the field intensity increase during the Levantine Iron Age anomaly (LIAA). In addition, these results are compatible with the paleointensities estimated by Monster et al. (2015) for the same lava-flow (Figure 9b), as Site 14, with both the Thellier-Thellier and Microwave methods (51.9 ± 4.0 μT and 52.0 ± 3.1 μT, respectively). A high-intensity anomaly of over 80 μT during that age has been previously reported in the Canary Islands by de Groot et al. (2015). Although the paleointensity value reported here does not reach such high values, it reinforces the presence of high intensities during the LIAA in this region. Unfortunately, no Thellier-type estimations could be obtained for the chronologically compatible site LPS08.

Sites LPS06 and LPS10, both with the same isotopic age, display intensity values lower than 30 μT, and reach 19.3 ± 6.0 μT for LTD-Thellier in LPS06. Considering age uncertainties, these low values are better correlated with the younger moderate intensity minimum produced around 6.2 ka. Keeping in mind the age uncertainty, this drop in intensity would not necessarily be accompanied by anomalous inclinations, although the SHA.DIF.14k model does show a marked inclination decrease during that period.

Site LPS09 displays a coherent paleointensity estimation according to the GGF100k model, although it also exhibits considerable uncertainty both in intensity and age. On the other hand, LPS04 with both Thellier-type methods in great coherency, points toward a relatively low intensity value (~30 μT). This is in good agreement with the expected field, which shows a slight intensity decrease during these ages, according to the Hilina Pali relative minimum (Di Chiara et al., 2025). Unfortunately, no paleointensity result could be obtained for the chronologically compatible site LPS02.

Sites LPS01 and LPS11 have similar ages (25 and 26 ka, respectively), and their paleointensity values agree. They display moderately low intensity values obtained through Thellier-type experiments (below 30 μT). Notably lower values (around 13 μT, VADM ~26 ZAm^2) are found in site LPS03 through both Thellier-type methods (Figure S2 in Supporting Information S1), consistent with a relative paleointensity minimum around 27 ka, not associated with a documented excursion. Although the paleomagnetic direction of this site displays expected values, this intensity represents a significantly low value, the lowest recorded in this study. The occurrence of this geomagnetic strength weakening might be related to the anomalous directions observed at the chronologically compatible site LPS11. While multiple global paleointensity stacks (e.g., GGF100k, Panovska et al., 2018; PADM2M, Ziegler et al., 2011; PISO-1500, Channell et al., 2009) show a moderate relative paleointensity minimum around 25–28 ka, this intensity drop, younger than the Mono Lake excursion (reported in the Canary Islands at ~33 ka; Kissel et al., 2011), has not been formally named. Site LPS05, with a poor coherency between methods, displays intensity values similar to the present-day field. The oldest site, LPS12, yields a moderately higher than the present-day field (46 μT). Its higher value relative to the GGF100k curve could be due to the smoothing inherent to sedimentary records, making a modest field increase during that time entirely plausible.

6. Conclusions

The comprehensive evaluation of rock magnetic behavior and paleointensity reliability in the 13 Quaternary studied lava flows yielded low-temperature oxidation as a primary source of paleointensity failure, inducing a TCRM viscous remanence and leading to paleointensity overestimation of many specimens subjected to the classic Thellier-Coe method. Many cases exhibited poor coherency of pTRM-checks, fostered by unstable magnetic components rather than thermal alteration.

Low temperature demagnetization pretreatment successfully reduced the magnetic viscosity contribution for paleointensity experiments, enhancing the signal of stable magnetic carriers. This fact highlights the significance of rock magnetic characterization and laboratory protocols in recovering robust paleointensity signals from volcanic records.

This study provides new paleomagnetic and paleointensity data over the last millennia in La Palma, covering most of the Late Pleistocene to prehistoric Holocene volcanic record in the island. The obtained results suggest the occurrence of relatively high intensities, chronologically at the same time as the LIAA observed in Europe, and the occurrence of a relative paleointensity minimum around 27 ka, not associated with any documented excursion.

Conflict of Interest

The authors declare no conflicts of interest relevant to this study.

Data Availability Statement

All the original data are available on the Zenodo online open access repository Vernet, 2025. The software used for interpretation of rock magnetic experiments are RockMag Analyzer 1.1 (Leonhardt, 2006), Cureval8 (Chadima & Hrouda, 2009) and FORCinel (Harrison & Feinberg, 2008). The software used for interpretation of paleomagnetic and paleointensity results are Remasoft (Chadima & Hrouda, 2006), PMagTools (Hounslow, 2006), ThellierTool 4.2 (Leonhardt & Krása, Krása, 2004) and Yamamoto et al.'s (2022) code in PmagPy software (Tauxe et al., 2016).

Acknowledgments
This research has been supported by projects PID2019105796GB-I00, PID2024-159094NB482-I00 of the Agencia Estatal de Investigación and BU037P23 of Junta de Castilla y León and the European Regional Development Fund. Eva Vernet Tarragó acknowledges funding from PRE2020-094803 (Agencia Estatal de Investigación) contract. This work was also supported by the project PID2022-136948NB-100/AEI/https://doi.org/10.13039/50110 00110 33/FEDER, UE (Spanish Ministry of Science and Innovation), and JSPS KAKENHI Grants JP21H01171 and JP24K00720. We would like to acknowledge Antonio González Morales agent of the environment protection of La Palma, for his great help during the sampling campaign. We would like also to thank Prof. S. Panovska for her great help with providing the full-vector data of GGF100k and ArchKalMag14k models. We sincerely appreciate the insightful comments provided by Editor Mark Dekkers, Associate Editor Bjarne Almqvist, Prof. Huapei Wang and an anonymous reviewer, which have greatly improved the manuscript. The authors confirm and agree that this research paper is a component of Eva Vernet's PhD thesis.

References

Almeida, T. P., Muxworthy, A. R., Kasama, T., Williams, W., Damsgaard, C., Frandsen, C., et al. (2015). Effect of maghemization on the magnetic properties of nonstoichiometric pseudo-single-domain magnetite particles. *Geochemistry, Geophysics, Geosystems*, *16*(9), 2969–2979. https://doi.org/10.1002/2015GC005858

Ancochea, E., Barrera, J. L., & Bellido, F. (2004). Canarias y el vulcanismo neógeno peninsular. *Geol. España*, *8*, 635–682.

Anguita, F., Fernández, C., Márquez, Á., León, R., & Casillas, R. (2025). The Canary hotspot revisited: Refutation of the Hawaii paradigm and an alternative, plate-based hypothesis. *Earth-Science Reviews*, *261*, 105038. https://doi.org/10.1016/j.earscirev.2024.105038

Barker, A., Troll, V., Carracedo, J., & Nicholls, P. (2015). The magma plumbing system for the 1971 Teneguía eruption on La Palma, Canary Islands. *Contributions to Mineralogy and Petrology*, *170*(5–6), 54. https://doi.org/10.1007/s00410-015-1207-7

Calvo-Rathert, M., Vernet, E., Parés, J. M., Soler, V., Sánchez-Moreno, E. M., Bógalo, M. F., et al. (2024). Reliability of the palaeomagnetic signal recorded in a lava flow erupted on 4 December 2021 in La Palma (Canary Islands, Spain). *Geophysical Journal International*, *239*(2), 841–861. https://doi.org/10.1093/gji/ggae297

Carracedo, J. C., Badiola, E. R., Guillou, H., de la Nuez, J., & Pérez Torrado, F. J. (2001). Geology and volcanology of La Palma and El Hierro, Western Canaries. *Estudios Geológicos*, *57*(5–6), 175–273. https://doi.org/10.3989/egeol.01575-6134

Chadima, M., & Hrouda, F. (2006). Remasoft 3.0 a user-friendly paleomagnetic data browser and analyzer [Software]. *Travaux Géophysiques*, *27*, 20–21.https://www.researchgate.net/publication/284652101_Remasoft_30_a_userfriendly_paleomagnetic_data_browser_and_analyzer

Chadima, M., & Hrouda, F. (2009). Cureval 8.0: Thermomagnetic Curve Browser for windows [Software]. Agico, Inc. https://www.agico.cz/text/software/cureval/cureval.php

Channell, J. E. T., Xuan, C., & Hodell, D. A. (2009). Stacking paleointensity and oxygen isotope data for the last 1.5 Myr (PISO-1500). *Earth and Planetary Science Letters*, *283*(1–4), 14–23. https://doi.org/10.1016/j.epsl.2009.03.012

Coe, R. S. (1967). Paleo-intensities of the Earth's magnetic field determined from Tertiary and Quaternary rocks. *Journal of Geophysical Research*, *72*(12), 3247–3262. https://doi.org/10.1029/JZ072i012p03247

Courtillot, V., Davaille, A., Besse, J., & Stock, J. (2003). Three distinct types of hotspots in the Earth's mantle. *Earth and Planetary Science Letters*, *205*(3–4), 295–308. https://doi.org/10.1016/S0012-821X(02)01048-8

Craig, J. R., & Vaughan, D. J. (1994). Ore mineral textures. In J. R. Craig & D. J. Vaughan (Eds.), *Ore microscopy and ore petrography* (pp. 120–163). John Wiley and Sons. Chapter 7.

Cromwell, G., Tauxe, L., Staudigel, S., & Ron, H. (2015). Paleointensity estimates from historic and modern Hawaiian lava flows using glassy basalt as a primary source material. *Physics of the Earth and Planetary Interiors*, *241*, 44–56. https://doi.org/10.1016/j.pepi.2014.12.007

Day, R., Fuller, M., & Schmidt, V. A. (1977). Hysteresis properties of titanomagnetites: Grain size and compositional dependence. *Journal of Geophysical Research*, *82*(7), 571–579. https://doi.org/10.1029/JB082i007p00571

de Groot, L. V., Béguin, A., Kosters, M. E., van Rijsingen, E. M., Struijk, E. L. M., Biggin, A. J., et al. (2015). High paleointensities for the Canary Islands constrain the Levant geomagnetic high. *Earth and Planetary Science Letters*, *419*, 154–167. https://doi.org/10.1016/j.epsl.2015.03.020

Demarest, H., Jr. (1983). Error analysis for the determination of tectonic rotation from paleomagnetic data. *Journal of Geophysical Research*, *88*(B5), 4321–4328. https://doi.org/10.1029/JB088iB05p04321

Di Chiara, A. (2019). *Paleo-secular variations of the geomagnetic field in Africa during Holocene: A Review*. Geological Society, London, Special Publications. 497. SP497-2019. https://doi.org/10.1144/SP497-2019-51

Di Chiara, A., Karloukovski, V., Maher, B. A., Van Daele, M., Van der Meeren, T., & Verschuren, D. (2025). A continuous 150-kyr record of geomagnetic field variations from Lake Chala, eastern equatorial Africa. *Geochemistry, Geophysics, Geosystems*, *26*(4), e2024GC011933. https://doi.org/10.1029/2024GC011933

Dunlop, D. J. (2014). High-temperature susceptibility of magnetite: A new pseudo-single-domain effect. *Geophysical Journal International*, *199*(2), 707–716. https://doi.org/10.1093/gji/ggu247

Dunlop, D. J., & Argyle, K. S. (1997). Thermoremanence, anhysteretic remanence and susceptibility of submicron magnetites: Nonlinear field dependence and variation with grain size. *Journal of Geophysical Research*, *102*(B9), 20199–20210. https://doi.org/10.1029/97jb00957

Dunlop, D. J., & Özdemir, Ö. (2001). Beyond Néel's theories: Thermal demagnetization of narrow-band partial thermoremanent magnetizations. *Physics of the Earth and Planetary Interiors*, *126*(1–2), 43–57. https://doi.org/10.1016/S0031-9201(01)00243-6

Egli, R. (2021). Magnetic characterization of geologic materials with first-order reversal curves. In V. Franco & B. Dodrill (Eds.), *Magnetic measurement techniques for materials characterization*. Springer. https://doi.org/10.1007/978-3-030-70443-8_17

Guillou, H., Carracedo, J., & Day, S. J. (1998). Dating of the Upper Pleistocene-Holocene volcanic activity of La Palma using the unspiked K-Ar technique. *Journal of Volcanology and Geothermal Research*, *86*(1–4), 137–149. https://doi.org/10.1016/s0377-0273(98)00074-2

Guillou, H., Carracedo, J., & Duncan, R. (2001). K-Ar,40Ar/39Ar Ages and Magnetostratigraphy of Brunhes and Matuyama Lava Sequences from La Palma Island. *Journal of Volcanology and Geothermal Research*, *106*(3–4), 175–194. https://doi.org/10.1016/s0377-0273(00)00294-8

Haggerty, S. E. (1976). Oxidation of opaque mineral oxides in basalts. In D. Rumble (Ed.), *Oxide Minerals (Reviews in Mineralogy* (Vol. 3, pp. Hg1–Hg100). Mineralogical Society of America. Chapter 4.

Haggerty, S. E. (1991). Oxide textures-a mini-atlas. *Oxide minerals: petrologic and magnetic significance*, *25*, 129–219.

Harrison, R. J., & Feinberg, J. M. (2008). FORCinel: An improved algorithm for calculating first-order reversal curve distributions using locally weighted regression smoothing [Software]. *Geochemistry, Geophysics, Geosystems*, *9*(5). https://doi.org/10.1029/2008gc001987

Hounslow, M. W. (2006). PMagTools (Version 4.2a) [Software]. https://www.lancaster.ac.uk/staff/hounslow/resources/software/pmagtool.htm

Jackson, M., & Bowles, J. (2018). Malleable Curie temperatures of natural titanomagnetites: Occurrences, modes, and mechanisms. *Journal of Geophysical Research: Solid Earth*, *123*(2), 921–940. https://doi.org/10.1002/2017JB015193

Jackson, M., & Worm, H. U. (2001). Anomalous unblocking temperatures, viscosity and frequency-dependent susceptibility in the chemically remagnetized Trenton limestone. *Physics of the Earth and Planetary Interiors*, *126*(1–2), 27–42. https://doi.org/10.1016/s0031-9201(01)00242-4

Jeong, D., Liu, Q., Yamamoto, Y., Yu, Y., Zhao, X., & Qin, H. (2021). New criteria for selecting reliable Thellier-type paleointensity results from the 1960 Kilauea lava flows, Hawaii. *Earth Planets and Space*, *73*(1), 144. https://doi.org/10.1186/s40623-021-01473-6

Kirschvink, J. L. (1980). The least-squares line and plane and the analysis of palaeomagnetic data. *Geophysical Journal of the Royal Astronomical Society*, *62*(3), 699–718. https://doi.org/10.1111/j.1365-246X.1980.tb02601.x

Kissel, C., Guillou, H., Laj, C., Carracedo, J. C., Nomade, S., Pérez-Torrado, F., & Wandres, C. (2011). The Mono Lake excursion recorded in phonolitic lavas from Tenerife (Canary Islands): Paleomagnetic analyses and coupled K/Ar and Ar/Ar dating. *Physics of the Earth and Planetary Interiors*, *187*(3–4), 232–244. https://doi.org/10.1016/j.pepi.2011.04.014

Kissel, C., Laj, C., Rodriguez-Gonzalez, A., Perez-Torrado, F., Carracedo, J. C., & Wandres, C. (2015). Holocene geomagnetic field intensity variations: Contribution from the low latitude Canary Islands site. *Earth and Planetary Science Letters*, *430*, 178–190. https://doi.org/10.1016/j.epsl.2015.08.005

Kissel, C., Rodriguez-Gonzalez, A., Laj, C., Perez-Torrado, F., Carracedo, J. C., Wandres, C., & Guillou, H. (2015). Paleosecular variation of the earth magnetic field at the Canary Islands over the last 15 ka. In *Earth and planetary science letters*. Elsevier BV. https://doi.org/10.1016/j.epsl.2014.12.031

Kitahara, Y., Yamamoto, Y., Ohno, M., Kuwahara, Y., Kameda, S., & Hatakeyama, T. (2018). Archeointensity estimates of a tenth century kiln: First application of the Tsunakawa– Shaw paleointensity method to archaeological relics. *Earth Planets and Space*, *70*(1), 79. https://doi.org/10.1186/s40623-018-0841-5

Klügel, A., Hansteen, T. H., & Galipp, K. (2005). Magma storage and underplating beneath Cumbre Vieja volcano, La Palma (Canary Islands). *Earth and Planetary Science Letters*, *236*(1–2), 211–226. https://doi.org/10.1016/j.epsl.2005.04.006

Kontny, A., & Grothaus, L. (2017). Effects of shock pressure and temperature on titanomagnetite from ICDP cores and target rocks of the El'gygytgyn impact structure, Russia. *Studia Geophysica et Geodaetica*, *61*(1), 162–183. https://doi.org/10.1007/s11200-016-0819-3

Larson, E., Ozima, M., Ozima, M., Nagata, T., & Strangway, D. (1969). Stability of remanent magnetization of igneous rocks. *Geophysical Journal International*, *17*(3), 263–292. https://doi.org/10.1111/j.1365-246x.1969.tb00237.x

Leonhardt, R. (2006). Analyzing rock magnetic measurements: The RockMagAnalyzer 1.0 software [Software]. *Computers & Geosciences*, *32*(9), 1420–1431. https://doi.org/10.1016/j.cageo.2006.01.006

Leonhardt, R., Heunemann, C., & Krása, D. (2004). Analyzing absolute paleointensity determinations: Acceptance criteria and the software ThellierTool4.0 [Software]. *Geochemistry, Geophysics, Geosystems*, *5*. https://doi.org/10.1029/2004GC000807.Q12016.

Magli, A., Del Carlo, P., Di Roberto, A., Giordano, G., Meletlidis, S., Pompilio, M., & Speranza, F. (2025). Age-clustered eruptive activity at La Palma (Canary Islands) during the last 4000 years: Evidence from paleomagnetic dating. *Journal of Volcanology and Geothermal Research*, *462*, 108328. https://doi.org/10.1016/j.jvolgeores.2025.108328

Monster, M., de Groot, L. V., Biggin, A. J., & Dekkers, M. J. (2015). The performance of various palaeointensity techniques as a function of rock magnetic behaviour – A case study for La Palma. *Physics of the Earth and Planetary Interiors*, *242*, 36–49. https://doi.org/10.1016/j.pepi.2015.03.004

Monster, M. W. L., van Galen, J., Kuiper, K. F., Dekkers, M. J., & de Groot, L. V. (2018). A Late-Quaternary full-vector geomagnetic record from El Golfo section, El Hierro, Canary Islands. *Geophysical Journal International*, *215*(3), 1701–1717. https://doi.org/10.1093/gji/ggy361

Muxworthy, A., Turney, J., Qi, L., Baker, E., Perkins, J., & Abdulkarim, M. (2023). Interpreting high-temperature magnetic susceptibility data of natural systems. *Frontiers in Earth Science*, *11*, 1171200. https://doi.org/10.3389/feart.2023.1171200

Muxworthy, A. R. (1999). Low-temperature susceptibility and hysteresis of magnetite. *Earth and Planetary Science Letters*, *169*(1–2), 51–58. https://doi.org/10.1016/S0012-821X(99)00067-9

Nilsson, A., Holme, R., Korte, M., Suttie, N., & Hill, M. (2014). Reconstructing Holocene geomagnetic field variation: New methods, models and implications. *Geophysical Journal International*, *198*(1), 229–248. https://doi.org/10.1093/gji/ggu120

Panovska, S., Constable, C. G., & Korte, M. (2018). Extending global continuous geomagnetic field reconstructions on timescales beyond human civilization. *Geochemistry, Geophysics, Geosystems*, *19*(12), 4757–4772. https://doi.org/10.1029/2018GC007966

Paterson, G. A. (2011). A simple test for the presence of multidomain behavior during paleointensity experiments. *Journal of Geophysical Research*, *116*(B10), B10104. https://doi.org/10.1029/2011JB008369

Paterson, G. A., Tauxe, L., Biggin, A. J., Shaar, R., & Jonestrask, L. C. (2014). On improving the selection of Thellier-type paleointensity data. *Geochemistry, Geophysics, Geosystems*, *15*(4), 1180–1192. https://doi.org/10.1002/2013GC005135

Pavón-Carrasco, F. J., Osete, M. L., Torta, J. M., & De Santis, A. (2014). A geomagnetic field model for the Holocene based on archaeomagnetic and lava flow data. *Earth and Planetary Science Letters*, *388*, 98–109. https://doi.org/10.1016/j.epsl.2013.11.046

Pike, C. R., Roberts, A. P., & Verosub, K. L. (1999). Characterizing interactions in fine magnetic particle systems using first order reversal curves. *Journal of Applied Physics*, *85*(9), 6660–6667. https://doi.org/10.1063/1.370176

Pullaiah, G., Irving, E., Buchan, K. L., & Dunlop, D. J. (1975). Magnetization changes caused by burial and uplift. *Earth and Planetary Science Letters*, *28*(2), 133–143. https://doi.org/10.1016/0012-821x(75)90221-6

Qi, K., Cai, S., Qin, H., Yamamoto, Y., Deng, C., Pan, Y., et al. (2024). The culprit of bias for paleointensity estimation in the shaw-type protocol and an innovative calculation method. *Geophysical Research Letters*, *51*(14), e2024GL109930. https://doi.org/10.1029/2024gl109930

Qin, H., He, H., Liu, Q., & Cai, S. (2011). Palaeointensity just at the onset of the cretaceous normal superchron. *Physics of the Earth and Planetary Interiors*, *187*(3–4), 199–211. https://doi.org/10.1016/j.pepi.2011.05.009

Roberts, A. P., Pike, C. R., & Verosub, K. L. (2000). First-order reversal curve diagrams: A new tool for characterising the magnetic properties of natural samples. *Journal of Geophysical Research*, *105*(B12), 28461–28475. https://doi.org/10.1029/2000jb900326

Schanner, M., Korte, M., & Holschneider, M. (2022). ArchKalmag14k: A Kalman-filter based global geomagnetic model for the Holocene. *Journal of Geophysical Research: Solid Earth*, *127*(2), e2021JB023166. https://doi.org/10.1029/2021JB023166

Singer, B. S. (2014). A Quaternary geomagnetic instability time scale. *Quaternary Geochronology*, *21*, 29–52. https://doi.org/10.1016/j.quageo.2013.10.003

Smirnov, A. V., Kulakov, E. V., Foucher, M. S., & Bristol, K. E. (2017). Intrinsic paleointensity bias and the long-term history of the geodynamo. *Science Advances*, *3*(8), e1602306. https://doi.org/10.1126/sciadv.1602306

Smirnov, A. V., & Tarduno, J. A. (2005). Thermochemical remanent magnetization in Precambrian rocks: Are we sure the geomagnetic field was weak? *Journal of Geophysical Research*, *110*(B6), B06103. https://doi.org/10.1029/2004JB003445

Syono, Y., & Ishikawa, Y. (1963). Magnetocrystalline anisotropy of $xFe_2TiO_4{\cdot}(1\text{-}x)Fe_3O_4$. *Journal of the Physical Society of Japan*, *18*(8), 1231–1232. https://doi.org/10.1143/jpsj.18.1230

Tanaka, H., & Komuro, N. (2009). The Shaw paleointensity method: Can the ARM simulate the TRM alteration? *Physics of the Earth and Planetary Interiors*, *173*(3–4), 269–278. https://doi.org/10.1016/j.pepi.2009.01.003

Tanaka, H., & Yamamoto, Y. (2016). Palaeointensities from Pliocene lava sequences in Iceland: Emphasis on the problem of Arai plot with two linear segments. *Geophysical Journal International*, *205*(2), 694–714. https://doi.org/10.1093/gji/ggw031

Tauxe, L., Cromwell, G., de Groot, L. V., & Jarboe, N. (2021). Understanding nonideal paleointensity recording in igneous rocks: Insights from aging experiments on lava samples and the causes and consequences of fragile curvature in arai plots. *Journal of Geophysical Research: Solid Earth*, *126*(2), e2020JB020482. https://doi.org/10.1029/2020JB020482

Tauxe, L., Shaar, R., Jonestrask, L., Swanson-Hysell, N. L., Minnett, R., Koppers, A. A. P., et al. (2016). PmagPy: Software package for paleomagnetic data analysis and a bridge to the Magnetics Information Consortium (MagIC) database [Software]. *Geochemistry, Geophysics, Geosystems*, *17*(6), 2450–2463. https://doi.org/10.1002/2016GC006307

Thellier, E., & Thellier, O. (1959). Sur L'intensite de champ magnetique terrestre dans le passe historique et geologique. *Annales de Geophysique*, *15*, 285–376.

Vahle, C., & Kontny, A. (2005). The use of field dependence of AC susceptibility for the interpretation of magnetic mineralogy and magnetic fabrics in the HSDP-2 basalts, Hawaii. *Earth and Planetary Science Letters*, *238*(1–2), 110–129. https://doi.org/10.1016/j.epsl.2005.07.010

Valet, J. P., & Soler, V. (1999). Magnetic anomalies of lava fields in the Canary Islands. Possible consequences for paleomagnetic records. *Physics of the Earth and Planetary Interiors*, *115*(2), 109–118. https://doi.org/10.1016/S0031-9201(99)00071-0

Van den Bogaard, P. (2013). The origin of the Canary Islands Seamount Province – New ages of old seamounts. *Scientific Reports*, *3*(1), 2107. https://doi.org/10.1038/srep02107

Vernet, E. (2025). Raw data of La Palma Sur paleomagnetic and paleointensity study (Version 1) [Dataset]. *Zenodo*. https://doi.org/10.5281/zenodo.15634577

Wang, H., & Kent, D. V. (2013). A paleointensity technique for multidomain igneous rocks. *Geochemistry, Geophysics, Geosystems*, *14*(10), 4195–4213. https://doi.org/10.1002/ggge.20248

Wang, S., Chang, L., Tao, C., Bilardello, D., Liu, L., & Wu, T. (2021). Seafloor magnetism under hydrothermal alteration: Insights from magnetomineralogy and magnetic properties of the Southwest Indian Ridge basalts. *Journal of Geophysical Research: Solid Earth*, *126*(12), e2021JB022646. https://doi.org/10.1029/2021JB022646

Yamamoto, Y. (2006). Possible TCRM acquisition of the Kilauea 1960 lava, Hawaii: Failure of Thellier paleointensity determination inferred from equilibrium temperature of the Fe-Ti oxide, Earth Planet. *Space*, *58*(8), 1033–1044. https://doi.org/10.1186/bf03352608

Yamamoto, Y., Tauxe, L., Ahn, H., & Santos, C. (2022). Absolute paleointensity experiments on aged thermoremanent magnetization: Assessment of reliability of the Tsunakawa-Shaw and other methods with implications for "fragile" curvature. *Geochemistry, Geophysics, Geosystems*, *23*(4), e2022GC010391. https://doi.org/10.1029/2022GC010391

Yamamoto, Y., Torii, M., & Natsuhara, N. (2015). Archeointensity study on baked clay samples taken from the reconstructed ancient kiln: Implication for validity of the Tsunakawa-Shaw paleointensity method. *Earth Planets and Space*, *67*(1), 63. https://doi.org/10.1186/s40623-015-0229-8

Yamamoto, Y., & Tsunakawa, H. (2005). Geomagnetic field intensity during the last 5 Myr: LTD-DHT Shaw palaeointensities from volcanic rocks of the Society lslands, French Polynesia. *Geophysical Journal International*, *162*(1), 79–114. https://doi.org/10.1111/j.1365-246x.2005.02651.x

Yamamoto, Y., Tsunakawa, H., & Shibuya, H. (2003). Paleointensity study of the Hawaiian 1960 lava: Implications for possible causes of erroneously high intensities. *Geophysical Journal International*, *153*(1), 263–276. https://doi.org/10.1046/j.1365-246x.2003.01909.x

Ziegler, L. B., Constable, C. G., Johnson, C. L., & Tauxe, L. (2011). PADM2M: A penalized maximum likelihood model of the 0–2 Ma palaeomagnetic axial dipole moment. *Geophysical Journal International*, *184*(3), 1069–1089. https://doi.org/10.1111/j.1365-246X.2010.04905.x